Mechanical Systems and Signal Processing 256 (2026) 114500

Contents lists available at ScienceDirect

Mechanical Systems and Signal Processing

journal homepage: www.elsevier.com/locate/ymssp

Full length article

A CRLB-based statistical framework for interpreting diffraction-limited localization in Lamb wave array imaging

Tingjian Li [b,c], Shanwu Li [a], Shengbo Shan [d], Li Cheng [b], Yongchao Yang [a,*]

[a] School of Civil Engineering, Harbin Institute of Technology, Harbin, 150090, China
[b] Department of Mechanical Engineering, The Hong Kong Polytechnic University, Hong Kong, China
[c] College of Engineering, Eastern Institute of Technology, Ningbo, 315200, China
[d] College of Intelligent Science and Technology, National University of Defense Technology, Changsha, 410073, China

ARTICLE INFO

Communicated by J. Baqersad

Keywords:
Ultrasonic array imaging
Diffraction limit
Lamb waves
Total focusing method
Cramér–Rao lower bound

ABSTRACT

Ultrasonic phased array imaging based on Lamb waves offers accurate defect localization in non-destructive testing, where multimodal dispersion improves responsiveness to structural anomalies. As the classical technique, the delay-and-sum (DAS) beamforming algorithm is distinguished by its computational efficiency and robustness to noise; it is further improved by the total focusing method (TFM) which synthetically focuses at every point in the imaging region, thereby maximizing spatial resolution and defect detectability across the entire field. However, the resolution of TFM imaging, as with any other array imaging, is fundamentally constrained by the diffraction limit, prescribed by Rayleigh's criterion. Moreover, its effectiveness may be obscured by the multi-mode propagation of Lamb waves which introduces mode interference and overlapping wavefronts. Seeking to understand and quantify the fundamental factors governing imaging resolution and the inherent limitations in Lamb wave-based beamforming detection is therefore crucial to enhance TFM defect localization performance. In this study, we derive the Cramér–Rao lower bound (CRLB) for defect localization under a classical envelope-based, group-delay Lamb-wave DAS/TFM model. The resulting bound is interpreted as a statistical, model-conditioned benchmark for localization uncertainty of guided-wave imaging. Notably, under the adopted imaging formulation, the CRLB is found to follow the same principal wavelength-aperture trends with diffraction-limited point spread function (PSF) broadening, thereby providing an interpretable basis for comparing the localization behaviors of *multi-modal* Lamb wave. Extensive numerical simulations and experimental study are conducted; the results are observed to be consistent with these theoretical derivations. Particularly, the effect of different modes, including multi-modes, on the imaging resolution is studied; it is found that the introduction of the A_1 mode of Lamb waves provides the most substantial improvement in resolution, possibly because the A_1 mode exhibits higher group velocity, combined with its steeper dispersion curve slope, thereby enabling more precise and clearer resolution in detecting defects. Overall, this work contributes to a novel rigorous quantitative framework for understanding the resolution constraints in Lamb wave-based TFM and potentially in broader array imaging. The applicability of this work and further study needed in future research are also discussed.

* Corresponding author.
E-mail address: yangyongchao@hit.edu.cn (Y. Yang).

https://doi.org/10.1016/j.ymssp.2026.114500
Received 29 August 2025; Received in revised form 1 May 2026; Accepted 25 May 2026

1. Introduction

Ultrasonic Lamb waves, as guided elastic modes in thin-walled structures, exhibit remarkable sensitivity to mechanical condition changes, making them particularly advantageous for non-destructive testing (NDT) applications [1–6]. Their dispersive nature supports multiple coexisting modes, each interacting distinctively with structural features and defects, thereby enriching diagnostic capability. Moreover, their low attenuation enables efficient inspection of large or hard-to-access components, including aircraft wings, pipelines, and bridge decks [7–10].

Ultrasonic Lamb wave phased array imaging (ULWPAI), in particular, enables high-fidelity visualization of subsurface defects in plate-like structures by coherently focusing guided wave energy through beamforming [11,12]. This spatiotemporal control over wave propagation allows dynamic steering and focusing at arbitrary locations, enhancing sensitivity to damage while covering large areas [13,14]. Moreover, ULWPAI leverages multiple Lamb wave modes, exploiting their distinct propagation characteristics and long-range interactions to achieve flexible, high-resolution, and versatile non-destructive evaluation (NDE). [15–19]. Building upon the principles of ULWPAI, the total focusing method (TFM) leverages the full capture matrix (FCM), obtained from all transmit–receive combinations, to achieve synthetic focusing across the image [20–23]. Using the measured wavefield exhaustively, TFM maximizes spatial resolution and enhances signal-to-noise ratio (SNR), enabling superior defect detection and accurate visualization in complex structural systems [24].

Despite its advantages, the resolution of TFM, as with any other array imaging, is inherently constrained by the Rayleigh criterion (diffraction limit), which dictates that the minimum resolvable distance between two adjacent defects (scatters) is approximately half the wavelength of the propagating wave, as $\Delta x \approx \lambda/2$. When the separation between defects falls below this limit, conventional TFM struggles to distinguish closely spaced targets, compromising imaging accuracy [25–27]. Recently, a number of super-resolution TFM approaches have been proposed to *computationally* overcome this diffraction-limited behavior, including coherence-based weighting methods [28,29], sparsity-promoting or compressed-sensing reconstructions [30–32], and more recently deep-learning-based super-resolution strategies [33–36]. Besides, to overcome this resolution limitation, higher excitation frequencies, equivalent to smaller wavelength, may be used to achieve finer resolution. Thus, higher-order Lamb wave modes have been explored to enhance the resolution of defect detection capabilities by increased sensitivity to small and localized defects, e.g., local thickness variations and structural anomalies in corrosion defects of pipelines [37]. In addition, multi-mode Lamb wave propagation has also been exploited in numerical simulations, exhibiting enhanced accuracy and efficiency, particularly in thin-walled structures [38]. While their potentials are seen, these methods introduce additional challenges, including increased wave attenuation and the amplification of coherent noise and multiple scattering effects, which ultimately impose an upper limit on the usable frequency range [39].

Understanding how these physical constraints interact with the fundamental resolution limit of TFM imaging is essential. TFM imaging resolution is ultimately constrained by the diffraction limit, which defines the smallest resolvable feature based on the wavelength of the propagating wave. Considering the dispersion nature of Lamb waves, this relationship becomes inherently more complex: *each* propagating mode possesses a distinct wavelength and dispersion characteristic. Such multi-modal interactions may either degrade resolution through interference or enhance it by providing complementary information across modes. Understanding how modes influence the *effective* diffraction limit is therefore critical, not only for interpreting TFM imaging performance, but also for formulating optimal mode-selective processing strategies [40]. Such insights are essential for advancing imaging resolution beyond classical limits and unlocking the full potential of ULWPAI; however, a rigorous theoretical framework to enable such a capability is absent from existing research.

Given that multi-modal Lamb waves fundamentally modify the characteristics of the diffraction limit, this study thus seeks to establish a quantitative framework capable of disentangling the individual modal contributions and identifying the key parameters governing defect localization resolution. Specifically, we explore the rigorous theory of the Cramér–Rao lower bound (CRLB), which sets the theoretical lower limit on the variance of unbiased estimators, serving as a standard for evaluating estimator efficiency [41]. When an estimator's variance approaches the CRLB, it indicates near-optimal efficiency under given measurement conditions. In the context of Lamb wave-based sensing, CRLB analyses have been employed to evaluate the fundamental limits of parameter estimation [42]. Specifically, the CRLB has been formulated for thickness estimation in plate-like structures using full-field Lamb wave measurements, revealing a trade-off between frequency resolution and estimation accuracy [43]. Additionally, the CRLB has been derived for full-field displacement measurements to quantify the minimum achievable variance in displacement estimation, thereby defining the theoretical sensitivity limit of such measurements [44]. CRLB-based analyses have also been applied in Lamb-wave source localization [45,46] and in evaluating localization accuracy for FMC/TFM measurements [47–49]. These works demonstrate that CRLB offers an effective statistical tool for quantifying information limits in guided-wave sensing; however, its application has remained limited to specific estimation tasks rather than imaging resolution.

This study introduces a CRLB-based statistical framework for interpreting localization uncertainty in multi-modal Lamb-wave TFM. The analysis is intentionally developed for a classical envelope-based, group-delay imaging formulation, which provides a transparent benchmark for studying how wavelength, aperture, and modal content influence diffraction-related localization behavior. It is subsequently examined and supported through finite element simulations and laboratory experiments.

2. Methods

2.1. Total focusing method (TFM) and imaging resolution

As a representative array imaging (beamforming) method, the TFM is applied to process guided wave array data, serving as the foundation for initial defect visualization and subsequent quantitative resolution analysis. Given the dispersive and multi-modal

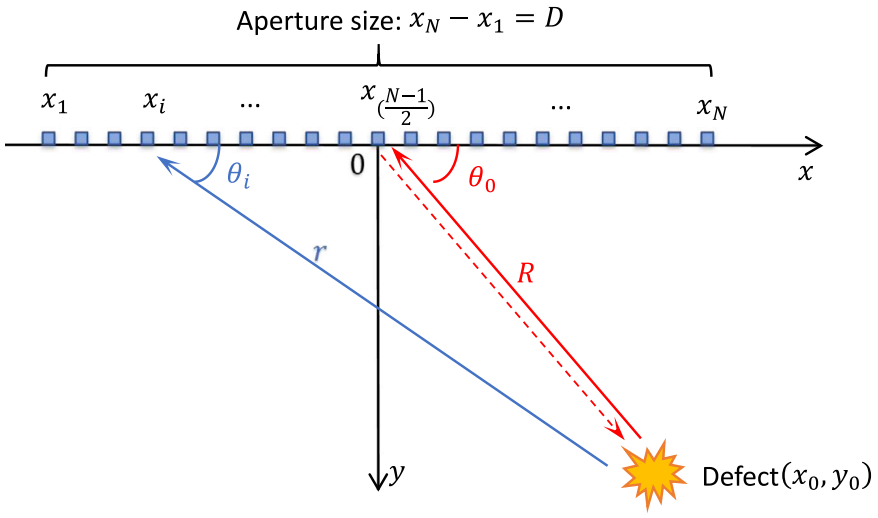

Fig. 1. Illustration of the total focusing method (TFM). The transducers highlighted in blue indicate the receivers.

nature of Lamb waves, TFM offers the flexibility to coherently reconstruct defect responses from multiple wave modes. This makes it particularly suitable for evaluating the spatial resolution of different modal components and establishing a unified framework for comparing their imaging performance. The schematic representation of a two-dimensional (2D) guided wave array alongside the principles of TFM beamforming is illustrated in Fig. 1. These x_i multiple measurement points collectively function as a receiver phased array. Once the guided wave array data is collected, a synthetic guided wave beam focusing is performed on each image pixel at (x, y) coordinates to generate a raw defect image denoted as $I(x, y)$ [25].

$$I = |\sum_{i=1}^{N} h_{ri}(\frac{\sqrt{x^2 + y^2} + \sqrt{(x_i - x_0)^2 + (y_i - y_0)^2}}{c_g})| \tag{1}$$

where $h_{ri}(t)$ represents the collected Lamb wave response at a specific time instance t at the receiver point located at(x_i, y_i), the point source defect at (x_0, y_0), and the excitation is performed using a transmitter positioned at the origin $(0, 0)$. N is the total number of receiver points, and c_g the group velocity of the incident guided wave mode. It is noted that the Lamb-wave signals are first mode-separated and bandpass filtered around the central frequency, yielding a narrowband waveform for each mode. Under this condition, the group-velocity–based delay law provides an accurate approximation and does not introduce noticeable phase defocusing. The computed image $I(x, y)$ is further processed by the TFM algorithm. The summation in Eq. (1) encompasses all possible transmitter–receiver combinations, accounting for every conceivable pairing. In this context, the pixel intensity of the image I at a specific coordinate (x, y) directly indicates the presence of a defect.

It is noted that Eq. (1) represents the standard single-transmitter, multi-receiver DAS formulation commonly used in guided-wave array imaging with scanning LDV or pitch–catch PZT setups [25,33]. In this configuration, a single actuator generates the Lamb wave, and the array aperture is synthesized entirely from the multiple receiver positions, leading to a summation only over receiver indices. This formulation is mathematically equivalent to a TFM reconstruction under a fixed excitation and differs from FMC-based TFM, which performs a double summation over all transmitter–receiver pairs. Importantly, the defect coordinates (x_0, y_0) in Eq. (1) are not assumed to be known; they simply denote the generic pixel location at which the TFM image is evaluated. During imaging, Eq. (1) is applied to every pixel within the reconstruction grid, and the defect location emerges naturally as the pixel that maximizes the TFM amplitude. Therefore, Eq. (1) is a forward model for image formation, instead of an expression that presumes prior knowledge of the defect position.

The attainable imaging resolution at the imaging point (x, y) in the TFM (and other array imaging methods) is constrained by the diffraction limit. In accordance with the Rayleigh criterion, the imaging lateral resolution, L_R, is expressed as:

$$L_R = \frac{0.61\lambda}{\sin\theta_R} \tag{2}$$

λ represents the wavelength of the selected Lamb wave mode, and θ the effective angular aperture of the imaging system, corresponding to the maximum angle between the incident and scattered wavefronts captured by the array elements (Fig. 1). Here, θ_R denotes the effective viewing angle spanned by the synthetic aperture. For a linear array, the PSF is sinc-like rather than Airy-like, and the constant 0.61 serves only as an approximate indicator of the diffraction-limited behavior rather than an exact value. The expression is therefore used for conceptual interpretation rather than as a strict model of the linear-array PSF. However, in guided-wave plate inspection, the effective aperture is typically much narrower due to the linear array geometry and mode-dependent directivity, so $\sin\theta_R < 1$ and the practical diffraction-limited resolution is therefore larger than 0.61λ.

Remark: The Rayleigh criterion provides a classical physical reference for diffraction-related PSF broadening in finite-aperture imaging. In the present work, the CRLB is introduced not to redefine this diffraction limit, but to provide a statistical interpretation of how diffraction-related spatial ambiguity manifests as localization uncertainty under the adopted envelope-based Lamb-wave TFM model.

2.2. Fisher information and the Cramér–Rao lower bound (CRLB)

The CRLB represents the theoretical lower limit on the variance of an estimator, providing a benchmark for the best achievable accuracy in parameter estimation; it is commonly used to assess the efficiency and accuracy of estimation methods. CRLB is computed through the Fisher information, which quantifies the amount of information that a measurement provides about the underlying parameters of its probability distribution. Let $\alpha = (\alpha_1, \dots \alpha_i)$ denote the vector of parameters to be estimated from measurements governed by the measurement model S, the likelihood of the measurement is represented as $f(S|\alpha)$; then the Fisher information is defined as:

$$\mathcal{I} = E\left(\left[\frac{\partial \ln(f(S|\alpha))}{\partial \alpha}\right]^{\dagger}\left[\frac{\partial \ln(f(S|\alpha))}{\partial \alpha}\right]\right) \tag{3}$$

where † denotes the Hermitian (complex conjugate transpose) operator. In the measurement model of the CRLB $S = S(\alpha) + W\left(\sigma^2\right)$ with an additive Gaussian white noise where $W \sim \mathcal{N}(0, \sigma^2)$, the Fisher information Eq. (3) simplifies to

$$[\mathcal{I}]_{(i,j)} = \frac{1}{\sigma^2}\left(\frac{\partial S}{\partial \alpha_i}\right)^{\dagger}\left(\frac{\partial S}{\partial \alpha_j}\right) \tag{4}$$

This study seeks to quantify, within the CRLB framework, the theoretical uncertainty of an estimator for the parameter α, based on observations derived from the measurement model S. We aim to derive the optimal estimator by employing the CRLB theorem, which asserts that an unbiased estimator can achieve the CRLB under the following relation:

$$\text{CRLB} = Var(\alpha^2) = \mathcal{I}^{-1} \tag{5}$$

Eq. (5) shows that the CRLB, defined as the inverse of the Fisher Information, characterizes the theoretical lower bound of parameter estimation variance in statistical inference.

In the subsequent sections, we extend this statistical principle to Lamb-wave TFM imaging and develop a CRLB-based framework for interpreting model-conditioned localization uncertainty.

3. Theoretical derivation of the CRLB for defect localization resolution in multi-mode lamb wave TFM imaging

3.1. Approximate and model-conditioned relation between CRLB-based localization uncertainty and diffraction-limited PSF broadening in TFM imaging

In TFM beamforming, the diffraction limit is classically characterized by the finite width of the PSF, which reflects the deterministic spatial ambiguity imposed by wavelength and aperture. By contrast, the CRLB quantifies the minimum achievable variance of an unbiased estimator under a specified measurement and noise model. In this work, the CRLB is introduced as a statistical tool to interpret how diffraction-induced PSF broadening translates into localization uncertainty under the adopted envelope-based narrowband TFM model.

In the context of TFM beamforming imaging, the Airy disk D_s defines the system's classical diffraction limit, representing the diffraction pattern formed when a point source is imaged through a finite aperture (Fig. 2). This limit is quantitatively given by the diameter of the central bright spot in the diffraction pattern. The Airy angle θ in the image plane is typically approximated as $sin\theta \approx 1.22\frac{\lambda}{D}$, where λ is the wavelength and D the aperture size. It corresponds to the distance between the central maximum and the first intensity minimum, marking the boundary beyond which two adjacent features become indistinguishable. From an estimation-theoretic perspective, the CRLB quantifies the minimum achievable variance of any unbiased estimator α, such as the estimated defect location (x_0, y_0) in TFM-based beamforming imaging. From an estimation-theoretic perspective, the square root of the CRLB gives the standard deviation of the localization error under the adopted measurement model. Under envelope-based narrowband focusing, both the PSF width and the CRLB are governed by the same delay-gradient structure. This motivates an approximate, model-conditioned scaling relation between diffraction-limited PSF broadening and CRLB-based localization uncertainty. For a defect located at $\mathbf{p}$:

$$\sqrt{\text{CRLB}_{\text{env}}(\mathbf{p})} \;\approx\; \kappa_{\text{env}}(\mathbf{p})\frac{0.61\lambda}{\sin\theta_R} \tag{6}$$

where $\kappa_{\text{env}}(\mathbf{p})$ is a model-dependent proportionality factor that depends on the adopted envelope-based narrowband measurement model, array geometry, effective aperture weighting, and estimator definition. Therefore, Eq. (6) should be interpreted as an approximate scaling law specific to the adopted envelope-based DAS/TFM formulation. It indicates that, within this model class, localization uncertainty follows the same principal wavelength and aperture trends as diffraction-limited PSF broadening. However, it depends on the signal model, noise level, array geometry, and estimator definition. The CRLB is thus used here as a statistical descriptor of diffraction-induced localization ambiguity.

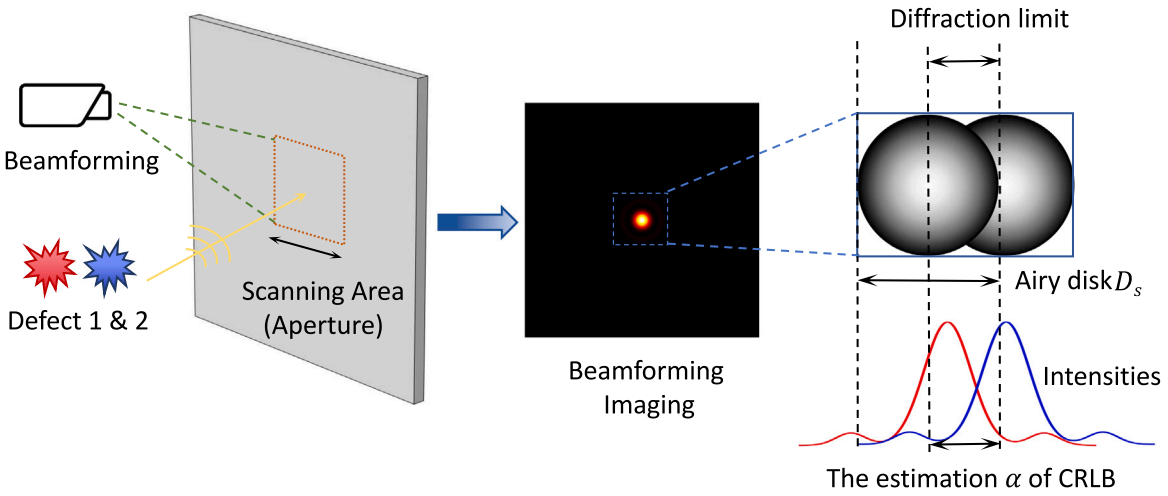

Fig. 2. Schematic illustration of the approximate, model-conditioned relation between diffraction-limited PSF broadening and CRLB-based localization uncertainty in envelope-based TFM imaging.

In TFM imaging, the PSF is formed through coherent backpropagation of time-delayed signals across a finite aperture. The finite width of the PSF main lobe does not arise from randomness or statistical uncertainty, but represents a deterministic spatial ambiguity imposed by wave diffraction and the limited aperture of the imaging system. This ambiguity reflects the fact that signals originating from nearby spatial locations cannot be perfectly distinguished by the imaging operator, even in the absence of noise.

For a point-like scatterer located at position $\mathbf{r}$, the TFM image intensity can be abstractly expressed as

$$I(\mathbf{r}) = \sum_{i=1}^{N} s_i\big(t - \tau_i(\mathbf{r})\big) \tag{7}$$

where $s_i(\cdot)$ denotes the received signal at the ith sensing points, $\tau_i(\mathbf{r})$ is the propagation delay associated with a hypothetical scatterer at position $\mathbf{r}$, and N is the number of receiver points. The spatial sharpness of the PSF is governed by how sensitively these delays vary with respect to spatial coordinates, i.e., by the gradient $\nabla_{\mathbf{r}}\tau_i(\mathbf{r})$.

From an estimation-theoretic perspective, defect localization relies on how sensitively the measured signals change with respect to small perturbations in the unknown scatterer position. For a measurement model with additive noise, the Fisher information matrix (FIM) associated with estimating $\mathbf{r}$ can be written as

$$\mathcal{I}(\mathbf{r}) = \frac{1}{\sigma^2}\sum_{i=1}^{N}\left(\frac{\partial s_i}{\partial \mathbf{r}}\right)^T\left(\frac{\partial s_i}{\partial \mathbf{r}}\right) \tag{8}$$

where σ^2 denotes the noise variance. For time-delay-based beamforming, the signal dependence on $\mathbf{r}$ is dominated by the propagation delay, such that

$$\frac{\partial s_i}{\partial \mathbf{r}} = \frac{\partial s_i}{\partial \tau_i}\cdot\frac{\partial \tau_i(\mathbf{r})}{\partial \mathbf{r}} \tag{9}$$

Substituting this relation into the Fisher information expression shows that the available Fisher information is fundamentally constrained by the squared magnitude of the delay gradient,

$$\mathcal{I}(\mathbf{r}) \propto \sum_{i=1}^{N}\left|\nabla_{\mathbf{r}}\tau_i(\mathbf{r})\right|^2 \tag{10}$$

Therefore, the same physical quantity that determines the spatial sharpness of the PSF also governs the Fisher information available for localization. The CRLB does not redefine the diffraction limit, but provides a statistical quantification of how this physically imposed spatial ambiguity translates into localization uncertainty in the presence of noise.

It is further noted that the Fisher information and the resulting CRLB explicitly depend on the spatial distribution of sensing points through the propagation delays $\tau_i(\mathbf{r})$. As indicated by the delay-gradient term $\nabla_{\mathbf{r}}\tau_i(\mathbf{r})$, the achievable localization precision is influenced by the effective aperture size, angular coverage, and sensor geometry associated with a given imaging configuration. The same analytical framework can be directly extended to alternative configurations, such as FMC-TFM or sparse PZT arrays, by appropriately redefining the propagation delays and measurement model. Accordingly, the present study focuses on the applicability of the proposed CRLB-based resolution analysis to classical beamforming-based imaging algorithms, providing a representative and interpretable baseline.

The CRLB derived in this study is based on the exact spherical-wave propagation model and is therefore valid in both Fresnel and far-field regimes. For a defect located at $\mathbf{p} = (x_0, y_0)$ and a receiver at $\mathbf{r}_i = (x_i, y_i)$, the propagation distance is

$$r_i(\mathbf{p}) = \|\mathbf{p} - \mathbf{r}_i\| \tag{11}$$

and the phase of the received Lamb-wave signal is given by

$$\phi_i(\mathbf{p}) = k\, r_i(\mathbf{p}) \tag{12}$$

where k denotes the modal wavenumber. This formulation does not rely on any far-field approximation and fully accounts for wavefront curvature.

The FIM for localization depends on the gradient of the signal with respect to the defect position,

$$\mathcal{I}(\mathbf{p}) = \frac{1}{\sigma^2} \sum_i \left(\frac{\partial s_i}{\partial \mathbf{p}} \right)^T \left(\frac{\partial s_i}{\partial \mathbf{p}} \right) \tag{13}$$

where $s_i(\mathbf{p}) = A\cos(kr_i(\mathbf{p}) + \phi_0)$. The position dependence enters solely through the distance $r_i(\mathbf{p})$, whose gradient is

$$\frac{\partial r_i}{\partial \mathbf{p}} = \frac{\mathbf{p} - \mathbf{r}_i}{\|\mathbf{p} - \mathbf{r}_i\|} \tag{14}$$

which is a unit direction vector independent of the propagation regime.

Consequently, the scaling of the Fisher information is governed by the wavenumber k and the angular diversity provided by the array aperture, rather than by whether the propagation occurs in the Fresnel or far-field regime. The far-field approximation corresponds to a linearization of $r_i(\mathbf{p})$ and may in fact reduce the available information by neglecting higher-order spatial variations. Therefore, the CRLB derived here represents a physically consistent localization bound under spherical-wave propagation and does not artificially benefit from near-field effects.

Let the received guided-wave signal at the ith sensor be expressed in its general broadband form as

$$x_i(t; \mathbf{p}) = s_i\big(t - \tau_i(\mathbf{p})\big) + n_i(t) \tag{15}$$

Phase-consistent beamformers, such as reverse time migration or dispersion-compensated TFM, operate directly on the broadband signals $x_i(t)$ and aim to coherently refocus the multimodal wavefield. In contrast, classical time-delay-based DAS/TFM formulations apply a group-velocity delay followed by envelope detection, yielding an effective measurement of the form

$$y_i(\mathbf{p}) = g\big(\tau_i(\mathbf{p})\big) + w_i \tag{16}$$

where $g(\cdot)$ represents the envelope of the received signal and w_i denotes effective noise. Since the envelope-based measurement y_i is obtained through a deterministic, parameter-independent transformation of the full broadband signal $x_i(t)$, the Fisher information satisfies the standard data processing inequality.

From an estimation-theoretic perspective, the envelope-based model can be interpreted as a linear transformation followed by a nonlinear magnitude operation applied to the original broadband measurements. The Fisher information associated with any unbiased estimator of $\mathbf{p}$ therefore satisfies

$$\mathcal{I}_{\text{env}}(\mathbf{p}) \preceq \mathcal{I}_{\text{full}}(\mathbf{p}) \tag{17}$$

where $\mathcal{I}_{\text{full}}$ denotes the Fisher information obtainable from the full phase-preserving broadband signals, and $\mathcal{I}_{\text{env}}$ corresponds to the envelope-based measurement model adopted in this work.

Accordingly, the Fisher information retained after envelope detection cannot exceed that available in the full phase-preserving broadband measurements. Provided that the corresponding Fisher information matrices are nonsingular, this implies:

$$\text{CRLB}_{\text{env}}(\mathbf{p}) \succeq \text{CRLB}_{\text{full}}(\mathbf{p}) \tag{18}$$

where CRLB_{env} denotes the localization bound associated with the adopted envelope-based, group-delay measurement model, and $\text{CRLB}_{\text{full}}$ denotes the bound that would be achievable from the full phase-preserving broadband signals. Eq. (18) emphasizes that the bound reported in this work should therefore be interpreted as a model-conditioned benchmark for classical envelope-based DAS/TFM, rather than as a universal physical limit for all Lamb-wave imaging operators.

Accordingly, the CRLB reported here should be interpreted as a localization bound conditioned on the envelope-based, group-delay measurement model. The present analysis provides a transparent and analytically tractable benchmark for understanding how array geometry and diffraction govern estimator performance within a widely used class of guided-wave imaging operators.

In the following, we derive the CRLB based on the underlying measurement model, providing a quantitative framework to characterize the defect localization precision governed by multi-mode Lamb wave propagation.

3.2. Analytical derivation of the CRLB for defect localization in multi-mode lamb wave measurement model

Building upon the approximate relation in Eq. (6) which is used here to interpret the scaling between diffraction-limited PSF broadening and localization uncertainty under the adopted envelope-based model, we next derive the CRLB for defect localization using an explicit array-based multi-mode Lamb-wave measurement model.

Under the assumption of an infinitely extended detection region free from boundary reflections, the full-field measurement of Lamb wave propagation is represented by the following measurement model:

$$S_{total} = \sum_{i=1}^{N}\sum_{j=1}^{M} A_{ij} \cdot \cos\left(k_j \cdot \sqrt{(x_i - x_0)^2 + (y_i - y_0)^2} + \varphi_i\right) + W\left(\sigma^2\right) \tag{19}$$

where, i denotes the receiver index in the array, and j indexes the Lamb wave modes. The defect is modeled as a point source located at (x_0, y_0), and the measurement pixel positions are given by (x_i, y_i). This point-source assumption facilitates the analysis of the system's spatial response and resolution characteristics. The wavenumber k_j corresponds to the jth Lamb wave mode and is determined from the dispersion relation. The parameters A_{ij} and φ_{ij} represent the mode-specific amplitude and phase, respectively. Additive Gaussian white noise $W(\sigma^2)$, with variance σ^2, is assumed to be spatially uncorrelated, consistent with typical random fluctuations from both the source and the receiver, as well as with full-field measurements in plate-like structures.

For imaging analysis, particular attention is given to the amplitude terms A_{ij}, which reflect the contribution of each mode. These modal amplitudes are extracted through separation in the spatial frequency (wavenumber) domain to isolate individual Lamb wave components. Mode separation is performed using a standard $f-k$ filtering procedure, in which the full wavefield is transformed to the spatial–temporal frequency domain and each mode is isolated by selecting its dispersion ridge in the $k-\omega$ plane. This approach yields mode-pure, narrowband signals which are then used in the subsequent CRLB analysis. While the methodology of mode decomposition is essential for interpreting imaging performance, however, a detailed discussion of this consideration extends beyond the scope of the current work.

By substituting the measurement model from Eq. (19) into the CRLB formulation, we lay the groundwork for deriving the theoretical limits of defect localization accuracy. This approach enables a quantitative evaluation of the minimum achievable variance in estimating defect positions (x_0, y_0) under noise, while also revealing the key factors that govern the resolution and performance of Lamb wave-based TFM imaging systems.

According to Eq. (3), if the Lamb wave has M modes, then the size of the FIM will be $(2M+3)\times(2M+3)$. We simplify the parameters as follows:

$$\beta_j = \begin{cases} A_j, 1 \le j \le M \\ \varphi_{j-M}, M+1 \le j \le 2M \end{cases} \tag{20}$$

and $\rho = \sqrt{\left(x_i - x_0\right)^2 + \left(y_i - y_0\right)^2}$. For each receiver we only estimate the following parameters: the amplitude A_j, the position (x_0, y_0) of the defect, the phase φ_j, and the variance of Gaussian white noise σ^2. According to Eq. (19), the full-field Lamb wave measurement at a single sensor can be expressed as:

$$S\left(A_j, x_0, y_0, \varphi_j, \sigma^2\right) = \sum_{j=1}^{M} A_j \cdot \cos\left(k_j \cdot \rho + \varphi_{j+M}\right) + W\left(\sigma^2\right) \tag{21}$$

To make the CRLB framework more applicable to practical NDT scenarios, we extend the simplified full-field Lamb wave measurement model S_{total} by incorporating three critical real-world factors: wave attenuation, material anisotropy, and boundary reflections. These effects, often encountered in practical applications, can substantially affect the signal model and therefore the estimation accuracy. The extended measurement signal model S_{total} received at sensor i is expressed as:

$$S_{total}^{(i)} = \sum_{j=1}^{M} A_j \cdot e^{-\alpha_j \cdot \rho} \cdot \cos\left(k_j \cdot \rho + \varphi_{j+M}\right) + \sum_{r=1}^{R} \Delta S_{ref}^{(i)} + W_i\left(\sigma^2\right) \tag{22}$$

where α_j is the frequency-dependent attenuation coefficient of mode j, the attenuation term accounts for the exponential decay of wave amplitude over distance, which is especially relevant for higher-frequency or higher-order modes; $\Delta S_{ref}^{(i)}$ represents the ith reflected wave component due to boundary reflections, which can be modeled as zero-mean Gaussian interference or treated via empirical attenuation scaling $N(0, \sigma_{ref}^2)$.

In this study, these effects are reconciled with the theoretical model as follows. First, dispersion and waveform distortion are mitigated through narrowband excitation and envelope-based time-of-flight extraction, such that the dominant propagation behavior can be effectively described by an equivalent group velocity. Residual dispersion effects that are not captured by this simplified representation contribute to deviations from the idealized model and are implicitly absorbed into the noise term. Second, attenuation primarily affects the signal amplitude and SNR, and is therefore reflected in the noise variance parameter of the CRLB formulation. Finally, reflections and boundary effects are mitigated through temporal windowing that isolates the first-arrival wave packet associated with the direct propagation path. As a result, reflected components are excluded from the localization model, and any remaining interference is treated as part of the effective noise.

This extended signal model improves physical realism by incorporating anisotropic propagation effects, attenuation, and boundary reflections, which factors often encountered in real-world ultrasonic NDT. Importantly, these additional terms can be directly included in the FIM, either analytically (for known attenuation profiles and dispersion) or numerically (using measured or simulated wavefields). In next section, we demonstrate through both finite element simulation and experiment that the CRLB derived under this extended model remains consistent with practical defect localization results, validating its physical robustness and applicability.

Then FIM in Eq. (22) becomes

$$\mathcal{I}\left(\beta_j, x_0, y_0, \sigma_{ref}^2, \sigma^2\right) = \frac{1}{\sigma_{ref}^2} \cdot \frac{1}{\sigma^2} \cdot \begin{pmatrix} \left(\frac{\partial S}{\partial x_0}\right)^{\dagger}\left(\frac{\partial S}{\partial x_0}\right) & \left(\frac{\partial S}{\partial x_0}\right)^{\dagger}\left(\frac{\partial S}{\partial \beta_1}\right) & \cdots & \left(\frac{\partial S}{\partial x_0}\right)^{\dagger}\left(\frac{\partial S}{\partial y_0}\right) \\ \left(\frac{\partial S}{\partial \beta_j}\right)^{\dagger}\left(\frac{\partial S}{\partial x_0}\right) & \left(\frac{\partial S}{\partial \beta_j}\right)^{\dagger}\left(\frac{\partial S}{\partial \beta_j}\right) & \cdots & \left(\frac{\partial S}{\partial \beta_j}\right)^{\dagger}\left(\frac{\partial S}{\partial y_0}\right) \\ \vdots & \vdots & \ddots & \vdots \\ \left(\frac{\partial S}{\partial y_0}\right)^{\dagger}\left(\frac{\partial S}{\partial x_0}\right) & \left(\frac{\partial S}{\partial y_0}\right)^{\dagger}\left(\frac{\partial S}{\partial \beta_j}\right) & \cdots & \left(\frac{\partial S}{\partial y_0}\right)^{\dagger}\left(\frac{\partial S}{\partial y_0}\right) \end{pmatrix} \tag{23}$$

Now, we need to calculate the partial derivatives that are present in the FIM. In this context, the main attention is paid to the diagonal entries in the estimator variance matrix, since they directly quantify uncertainty in estimates of individual parameters. In contrast, the off-diagonal terms, representing parameter covariances, are typically less emphasized in parameter influence evaluation. The following expressions are thus derived:

$$\frac{\partial S}{\partial \beta_j} = \begin{cases} e^{-\alpha_j \cdot \rho} \cdot \cos\left(k_j \cdot \rho + \beta_{j+M}\right), 1 \le j \le M \\ -\beta_{M-j} \cdot e^{-\alpha_j \cdot \rho} \cdot \sin\left(k_{j-M} \cdot \rho + \beta_j\right), M+1 \le j \le 2M \end{cases} \tag{24}$$

and

$$\frac{\partial S}{\partial x_0} = -\frac{x_0 - x_i}{\rho} \cdot \sum_{j=1}^{M} A_j \cdot e^{-\alpha_j \cdot \rho} \cdot \left[-\alpha_j \cdot \cos\left(k_j \cdot \rho + \varphi_{j+M}\right) - k_j \cdot \sin\left(k_j \cdot \rho + \varphi_{j+M}\right)\right] \tag{25}$$

Similarly we obtain a derivation for $\frac{\partial S}{\partial y_0} = \frac{y_0 - y_i}{\rho} \cdot \frac{\partial S}{\partial \rho}$, so we will only refer to x_0 in the following. To focus on the parameter of interest, we analytically eliminate auxiliary variables β_j such as amplitude A_j and phase φ_j, reducing the measurement model to a function of the defect location (x_0, y_0). It is effective to express the measurement at receiver i using a steering-vector model:

$$S_i(\mathbf{p}) \;=\; \sum_{j=1}^{M} c_j \, s_j(\rho; \mathbf{p}) + n_i \tag{26}$$

where $\mathbf{p} = (x_0, y_0)^{\top}$ denotes the defect location, $c_j = A_j e^{\mathrm{i}\phi_j}$ is the complex modal amplitude (containing both amplitude A_j and phase ϕ_j), $s_j(\rho; \mathbf{p})$ is the known (complex) modal response/steering term for mode j at receiver i (including propagation phase $e^{\mathrm{i}k_j\rho}$ and attenuation), and $n \sim \mathcal{N}(0, \sigma^2)$ denotes additive white Gaussian noise. Stack measurements into vector form $\mathbf{S} = [S_1, \ldots, S_N]^{\top}$ and define the complex design matrix $\tilde{G}(\mathbf{p}) \in \mathbb{C}^{N \times M}$ with entries $\tilde{G}_{i,j} = s_j(\rho; \mathbf{p})$; then denote the (vectorized) measurement at all receivers by $\mathbf{S} \in \mathbb{R}^N$ and suppose the model can be written in the form

$$\mathbf{S}(\mathbf{p}, \beta) = G(\mathbf{p})\,\beta + n \tag{27}$$

where β collects the (real-valued) amplitude/phase nuisance parameters (for complex amplitudes one may equivalently stack real and imaginary parts).

Under this model the partial derivatives entering the FIM are

$$\frac{\partial \mathbf{S}}{\partial \mathbf{p}} = \frac{\partial G(\mathbf{p})}{\partial \mathbf{p}}\,\beta, \qquad \frac{\partial \mathbf{S}}{\partial \beta} = G(\mathbf{p}) \tag{28}$$

Using Eq. (4) the full FIM (with parameter ordering $\theta = (\mathbf{p}^{\top}, \beta^{\top})^{\top}$) takes the block form

$$\mathbf{J}(\theta) \;=\; \frac{1}{\sigma^2}\begin{bmatrix} \mathbf{J}_{pp} & \mathbf{J}_{p\beta} \\ \mathbf{J}_{\beta p} & \mathbf{J}_{\beta\beta} \end{bmatrix} \tag{29}$$

with

$$\mathbf{J}_{pp} = \left(\frac{\partial \mathbf{S}}{\partial \mathbf{p}}\right)^{\top}\left(\frac{\partial \mathbf{S}}{\partial \mathbf{p}}\right), \quad \mathbf{J}_{p\beta} = \left(\frac{\partial \mathbf{S}}{\partial \mathbf{p}}\right)^{\top} G, \quad \mathbf{J}_{\beta\beta} = G^{\top}G \tag{30}$$

Treating β as nuisance parameters, the information relevant to $\mathbf{p}$ alone is obtained by eliminating β via the Schur complement, yielding the reduced Fisher matrix

$$\mathbf{J}_{pp}^{\mathrm{red}} \;=\; \mathbf{J}_{pp} \;-\; \mathbf{J}_{p\beta}\,\mathbf{J}_{\beta\beta}^{-1}\,\mathbf{J}_{\beta p} \tag{31}$$

The CRLB for the localization parameters is then given by the inverse of the reduced matrix,

$$\mathrm{Cov}(\hat{\mathbf{p}}) \geq \left(\mathbf{J}_{pp}^{\mathrm{red}}\right)^{-1} \tag{32}$$

and the scalar localization variance reported in the manuscript corresponds to the appropriate diagonal entries of $(\mathbf{J}_{pp}^{\mathrm{red}})^{-1}$.

It is noted that when complex amplitudes are used in the model, one may equivalently write β as the concatenation of real and imaginary parts; the Schur-complement elimination above applies in the same way. A few practical remarks follow: (i) to ensure numerical stability we compute the Moore–Penrose pseudoinverse of $\mathbf{J}$ (MATLAB implementation) when $\mathbf{J}_{\beta\beta}$ is ill-conditioned (e.g. strongly correlated modal responses); (ii) the complex-to-real stacking above doubles the nuisance-parameter dimension (giving the $(2M+3)\times(2M+3)$ matrix size when noise variance is included as an additional scalar parameter), and (iii) explicit expressions for the entries of $\mathbf{G}$ (e.g. $G_{i,j} = C\{e^{-\alpha_j\rho}e^{\mathrm{i}k_j\rho}\}$) can be substituted to compute the block matrices element-wise. This simplification enables a direct application of the FIM framework for estimating localization precision. The complete theoretical derivation is provided in Appendix A.

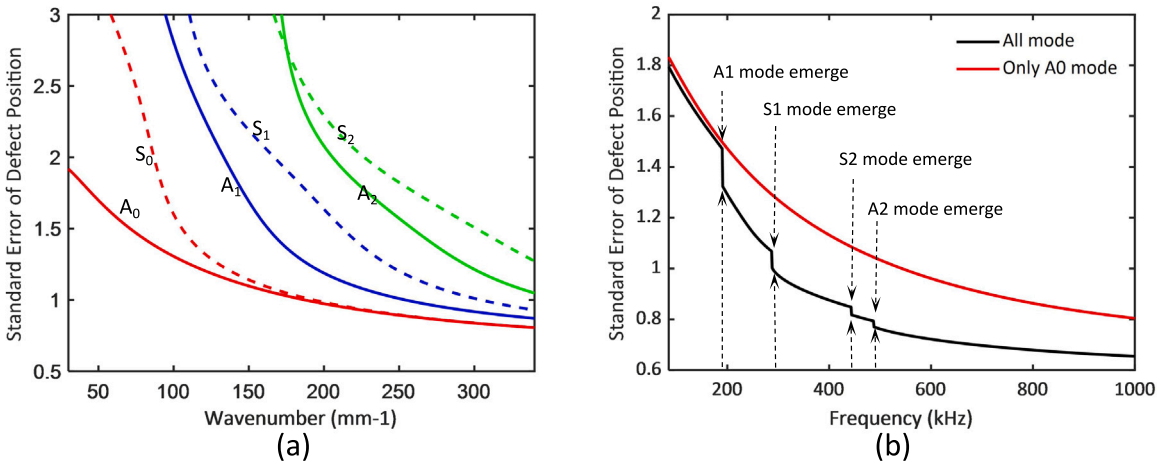

Fig. 3. (a) CRLB-derived standard deviation of defect localization plotted against wavenumber for different modes. The A_0 mode exhibits the lowest localization uncertainty at the same wavenumber, highlighting its favorable resolution characteristics in TFM imaging. (b) Frequency-dependent variation of CRLB in defect localization: Emergence of higher-order Lamb modes near cut-off frequencies enhances localization precision through reduced standard deviation.

3.3. Numerical evaluation of the CRLB for defect localization using multi-mode lamb wave measurements

Building upon the analytical derivation of the CRLB for defect localization, we adopt an array-driven multi-mode Lamb wave measurement model as the basis of our numerical investigation. The CRLB is evaluated by computing the Moore–Penrose pseudoinverse of the FIM in MATLAB, where the diagonal entry associated with (x_0, y_0) represents the minimum achievable localization variance under unbiased conditions. For interpretation, the square root of the CRLB is taken to yield the standard error of localization deviation, which provides a quantitative measure of the diffraction-limited resolution. This framework enables a direct evaluation of how different wave modes and their interactions influence the resolution limit under varying propagation conditions, as illustrated in Fig. 3(a). The vertical axis shows the standard error of defect localization derived from the CRLB, while the horizontal axis represents the wavenumber, which increases with excitation frequency and reflects the inverse of wavelength. To ensure a fair cross-mode comparison, the modal responses are normalized to have equal energy (unit amplitude) prior to evaluating the Fisher Information. This removes the trivial dependence on frequency-dependent amplitude variations and allows the CRLB to reflect intrinsic, mode-dependent information content rather than SNR differences across modes.

The CRLB-derived standard error of defect localization decreases with increasing Lamb wave wavenumber, which corresponds to higher excitation frequencies and shorter wavelengths, thus indicating improved spatial resolution. Among the considered modes, the A_0 mode consistently exhibits the lowest localization uncertainty at a given wavenumber, attributed to its high energy concentration and favorable dispersion characteristics. As excitation frequency rises and the localization performance of different modes begins to converge due to their increasingly similar wavenumbers.

Building on the CRLB analysis across individual modes, particularly the superior localization performance of the A_0 mode, it becomes essential to assess the impact of multi-mode fusion on the diffraction-limited resolution. While single-mode evaluations offer valuable insights, practical Lamb wave imaging inherently involves the simultaneous excitation and reception of multiple modes. In this context, a comprehensive CRLB framework enables quantitative comparisons between full-mode and single-mode imaging strategies.

To this end, we extend our analysis by incorporating the CRLB contributions from all available modes and compare the resulting localization bounds against those derived from the A_0 mode alone. As illustrated in Fig. 3(b), the activation of higher-order modes near their cut-off frequencies substantially decreases the CRLB-derived standard error, reflecting the additional information introduced by new modal branches. This reduction signifies an enhanced sensitivity to structural variations, highlighting the importance of frequency tuning to leverage modal diversity. Consequently, the multi-mode CRLB offers a quantitative and physically grounded perspective on the resolution limits of TFM imaging.

Moreover, Fig. 4 validate the consistency between theoretical predictions and numerical results. In Fig. 4(a), the CRLB decreases monotonically with increasing SNR, approaching the theoretical bound at high SNR. In Fig. 4(b), varying the empirical attenuation scaling at fixed SNR produces trends consistent with Fig. 3(b), while the activation of additional modes further reduces the CRLB. This agreement strengthens the model validation and highlights the complementary effects of noise reduction and modal diversity on achievable resolution. We account for multiple error sources more representative of practical NDT conditions, including noise-induced degradation, propagation attenuation, and structural inhomogeneity.

To further investigate how the emergence and selection of modes influence defect location performance, CRLB trends for various combinations of modes are computed and illustrated in Fig. 5(a). When all available modes are included, differences in

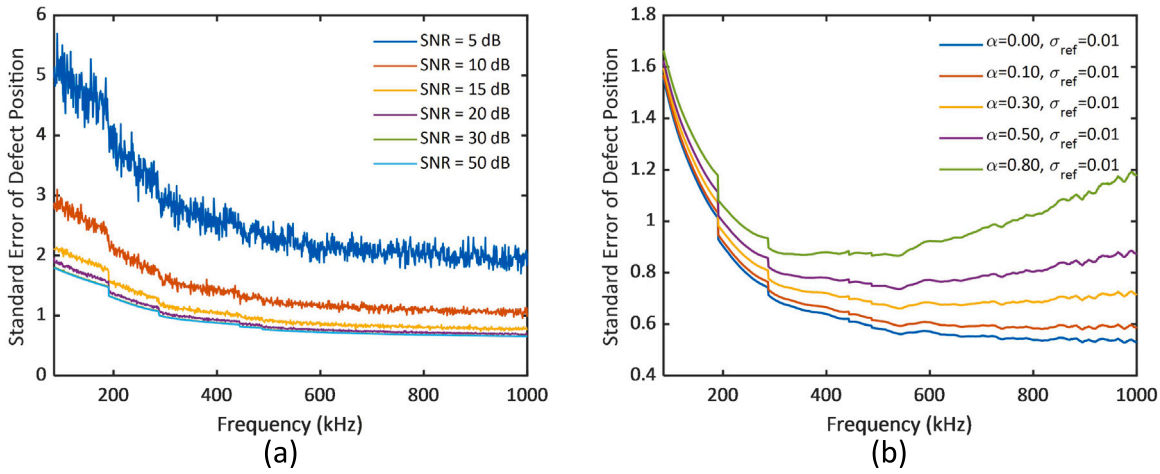

Fig. 4. (a) Relationship between CRLB and SNR. CRLB curves are plotted under a fixed attenuation coefficient for various SNRs, illustrating the effect of noise level on estimation accuracy: as SNR increases, the CRLB decreases. (b) Joint effect of SNR and attenuation coefficient on CRLB. CRLB curves are plotted for different empirical attenuation scaling factors α or their variance σ^2_{ref} under a fixed SNR, showing that stronger attenuation or greater uncertainty in attenuation increases the CRLB, indicating reduced estimation accuracy.

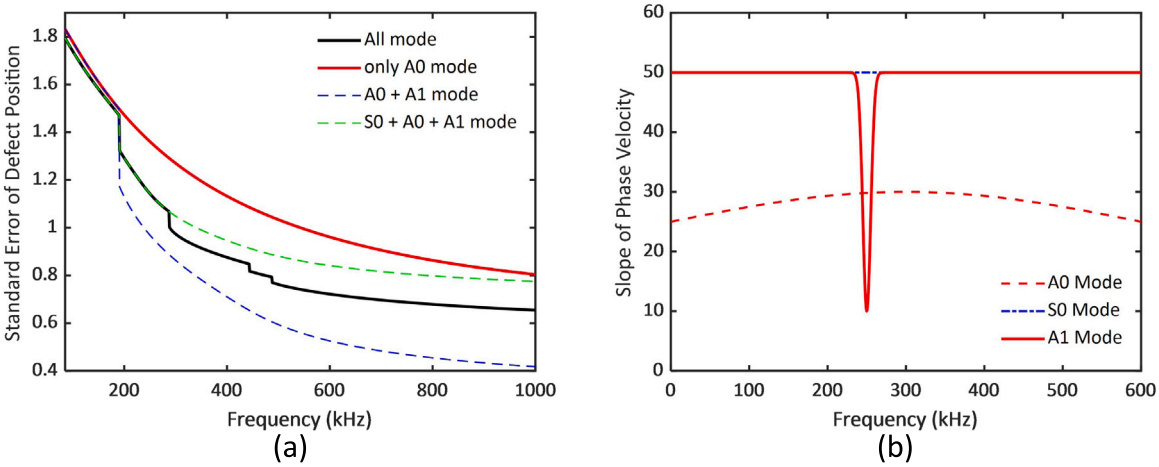

Fig. 5. (a) Frequency-dependent CRLB for defect localization: Combined use of antisymmetric modes ($A_0 + A_1$) yields the highest localization precision, while relying solely on (S_0) can degrade performance. (b) The slope of the Phase velocity when thickness is 8 mm. The A_1 mode shows the steepest improvement in localization precision near its cutoff frequency, highlighting its strong dispersion and high sensitivity to defect-induced structural changes at the onset of mode activation.

group velocities between symmetric and antisymmetric modes lead to phase mismatches. These mismatches cause constructive and destructive interferences that degrade waveform coherence and hinder accurate defect localization, resulting in elevated CRLB values. For multi–mode analyses, each Lamb-wave mode is focused using its own mode-dependent delay law, i.e., $h_{ri,j}(x,y) = \rho(x,y)/c_{g,j}$, where $c_{g,j}$ is the group velocity of mode j. When S- and A-family modes are combined coherently, their different phase velocities introduce a non-zero residual phase term after focusing, which results in the degradation. This phase mismatch is therefore inherently already incorporated in the model.

In contrast, constraining the analysis to antisymmetric modes $A_0 + A_1$ yields significantly reduced CRLB, indicating enhanced defect localization precision. This improvement arises from the complementary physical characteristics of the two modes: the A_1 mode exhibits strong sensitivity to local thickness variations, which promotes mode conversion into A_0 components. These A_0 waves, with their shorter wavelengths and higher wavenumbers, enhance spatial resolution and improve sensitivity to structural anomalies. Thus, this mode-selective approach offers a physically grounded strategy to optimize defect detectability in TFM imaging.

It is also observed that including the S_0 mode tends to compromise defect localization precision, as evidenced by elevated CRLB. This may be because its low dispersion and near-constant group velocity make it less responsive to localized structural changes such as small cracks or thinning, limiting its utility for precise defect localization. This observation is consistent with the slope of phase

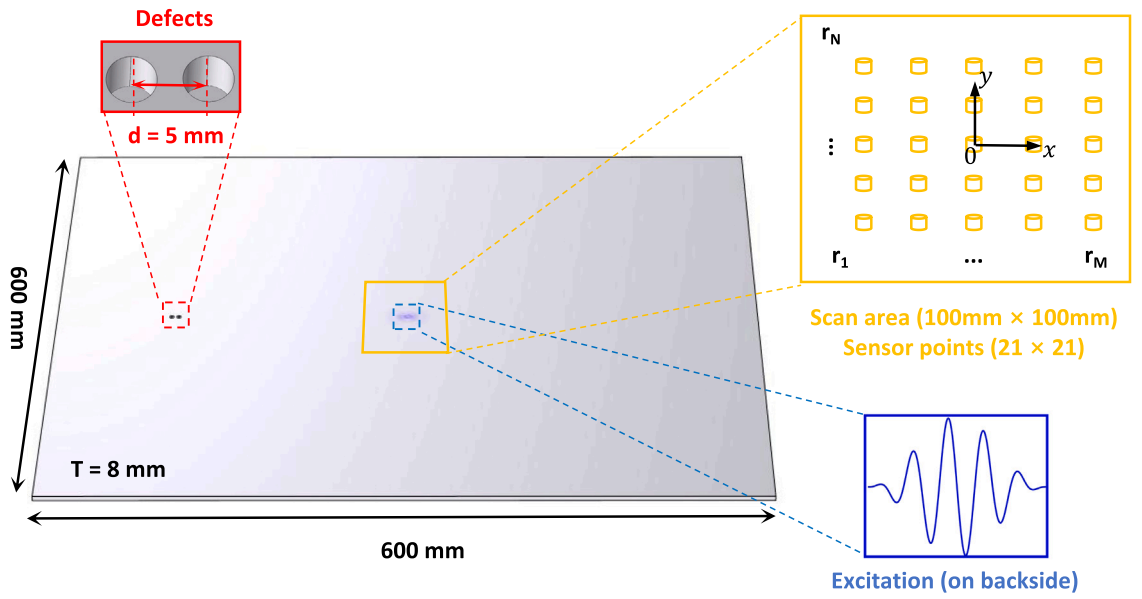

Fig. 6. Ultrasonic TFM phased array imaging simulation system: two hole defects are placed at a position 100 mm away from the left boundary. The distance between the centers of the two holes is 5 mm, the incident wave A_0 has a shortest wavelength of 12 mm. Based on Rayleigh's half-wavelength criterion, the 5 mm distance is smaller than the diffract limit 6 mm.

velocity as shown in Fig. 5(b), which clearly shows that the A_1 mode exhibits the steepest dispersion slope near its cut-off frequency. This implies a high rate of velocity change with frequency, making the mode particularly sensitive to medium perturbations.

Therefore, as observed, the A_1 mode provides improved imaging contrast and finer spatial resolution, yielding lower CRLB values for defect localization.

4. Finite element simulation and experimental validation

4.1. Finite element simulation

4.1.1. Axial two-target separability analysis for controlled benchmark

To validate the theoretical relationship between the CRLB of defect localization and the diffraction limit derived in the previous section, we conduct a TFM simulation using the finite element simulation software, COMSOL Multiphysics 6.0 (Fig. 6). The simulation parameters are set as follows: an aluminum plate with a thickness of 8 mm, excitation is performed at the back of the plate using a five-period Hanning window function with an excitation frequency of 260 kHz. The sensor array is positioned in the central 100 mm×100 mm area on the front surface of the plate, with a sensor spacing of 5 mm. At a position 100 mm away from the left boundary, two circular holes with a radius of 1 mm, a center distance of 5 mm, and a depth of 2 mm are set to simulate the defect.

The simulated plate is excited by a short burst centered at f = 260 kHz (five-cycle nominal burst, duration ≈ 19.2 μs). Giving one-way travel times from the defect (located at (0, 200 mm)) to a typical scan sensor (near $y = 0$) of roughly 0.2 m/c ≈ 37 μs (S_0) and 77 μs (A_0). To avoid contamination of the modal signals by edge reflections, a time window is selected which contains only the defect-scattered arrivals while excluding all plate-edge reflections. In the FEM model, the earliest edge reflections appear after approximately 200 μs, whereas the defect-reflected Lamb modes of interest arrive in the 100-180 μs range. Therefore, all modal separation and CRLB analyses are performed within the 100-200 μs window, which contains the complete defect-scattered wavefield but precedes any boundary reflections. We additionally verify numerically, by comparing the full recorded waveforms with extended time traces where no significant reflected energy enters this analysis window.

In the simulations, when using the excitation signal with a center frequency of 260 kHz, the wavelength of the S_0 mode is approximately 24 mm, and the wavelength of the A_0 mode is about 12 mm. The center-to-center spacing of the two circular hole defects d is 5 mm, which falls below the diffraction limit, which commonly defined as half the wavelength of the shortest incident wave $\lambda/2$ for the A_0 mode. For the two-target configuration at positions **p1** and **p2**, we construct the full measurement Jacobian with respect to all position and amplitude parameters. The unknown modal amplitudes are analytically eliminated using the Schur complement, resulting in a reduced Fisher information matrix associated only with the four position parameters (x_1, y_1, x_2, y_2). From the inverse of this reduced Fisher matrix, we obtain the marginalized covariance of the separation vector $\boldsymbol{\Delta p} = \mathbf{p2} - \mathbf{p1}$. We then evaluate the scalar separation uncertainty $\sigma_\Delta = \sqrt{tr(Cov(\boldsymbol{\Delta p}))/2}$, which corresponds to the standard deviation along the line joining the two defects. As a practical resolvability criterion, the two defects are declared unresolvable when the CRLB-predicted uncertainty

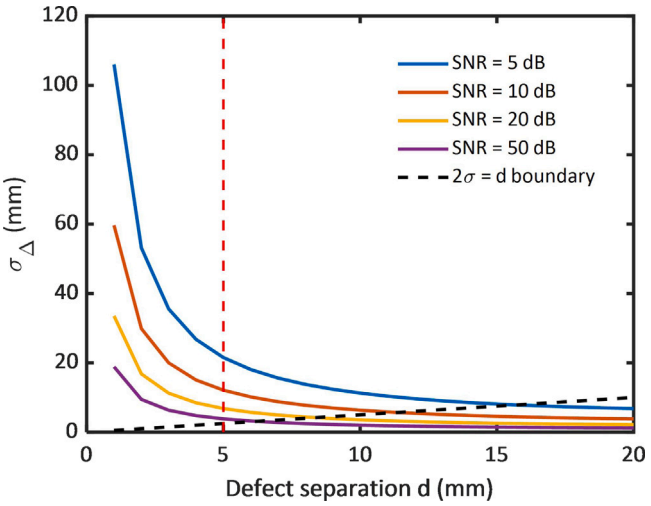

Fig. 7. CRLB-predicted resolvability of two closely-spaced defects. The dashed black line marks the practical resolution boundary $2\sigma_{\Delta} = d$, corresponding to the 95% Gaussian error diameter. Defect pairs lying above this boundary are fundamentally unresolvable, even under an ideal unbiased estimator. The results show that, at the experimentally relevant separation $d = 5$ mm, the CRLB predicts resolvability failure across all tested SNR levels, consistent with the observed diffraction-limited behavior.

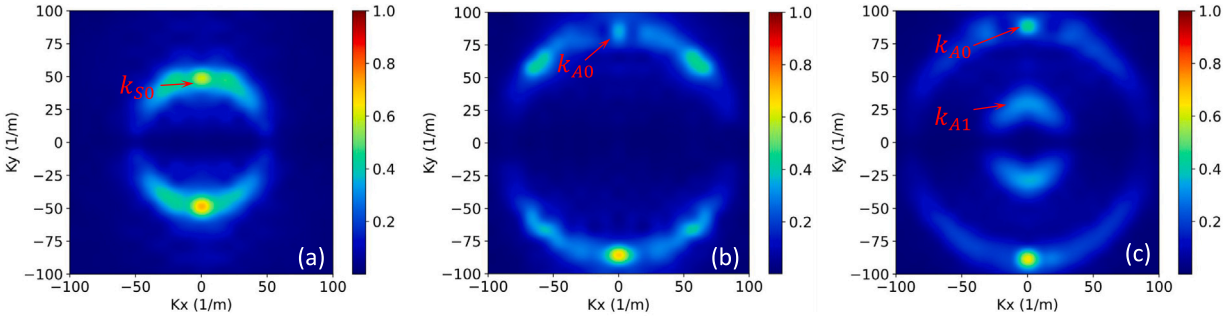

Fig. 8. Wavenumber spectrograms for (a) S_0 mode only, (b) A_0 mode only and (c) antisymmetric modes.

satisfies $2\sigma_{\Delta} \geq d$,meaning that the 95% Gaussian error diameter is comparable to or exceeds the true separation d. This resolvability test is performed across SNR values and defect separations to generate the curves in Fig. 7, which directly show whether the CRLB predicts resolvability failure under the stated experimental geometry and noise level. The figure therefore isolates the effect of SNR on the theoretical separability limit.

To further explore the physical mechanisms underlying the CRLB variation across different Lamb wave mode combinations, we performed a three-dimensional fast Fourier transform (3D-FFT) analysis on the acquired array data, as shown in Fig. 8. This operation enables clear separation of distinct modal components in the frequency–wavenumber–time domain. By applying appropriate bandpass filtering in the frequency–wavenumber domain, we isolated the S_0 mode, the A_0 mode, and their composite $(A_0 + A_1)$ signals. These filtered datasets were then transformed back into the time domain for subsequent waveform analysis.

Before performing full-field imaging, we examine the temporal interference characteristics of individual and combined Lamb wave modes using Hilbert envelope analysis. This allows us to assess how mode superposition influences the temporal resolution and SNR, both of which directly affect imaging accuracy and CRLB.

To quantify the temporal localization characteristics of each modal configuration, we selected a set of sensors aligned along a single propagation direction and analyzed their time-domain waveforms using Hilbert envelope transformation. The Hilbert transform allows the extraction of the analytic signal envelope, providing a smooth and physically interpretable representation of the signal's amplitude evolution over time.

For each sensor position, we compute the full width at half maximum (FWHM) of the envelope, defined as the temporal width between the two points where the envelope amplitude drops to 50% of its maximum [50]. This metric is commonly used in wave physics and signal processing as an indicator of temporal resolution and energy concentration. A smaller FWHM implies sharper wave packet localization, which directly corresponds to higher resolution and lower uncertainty in defect localization. To explain the connection between the temporal FWHM of the received Lamb-wave signals and the Fisher information, the following derivation

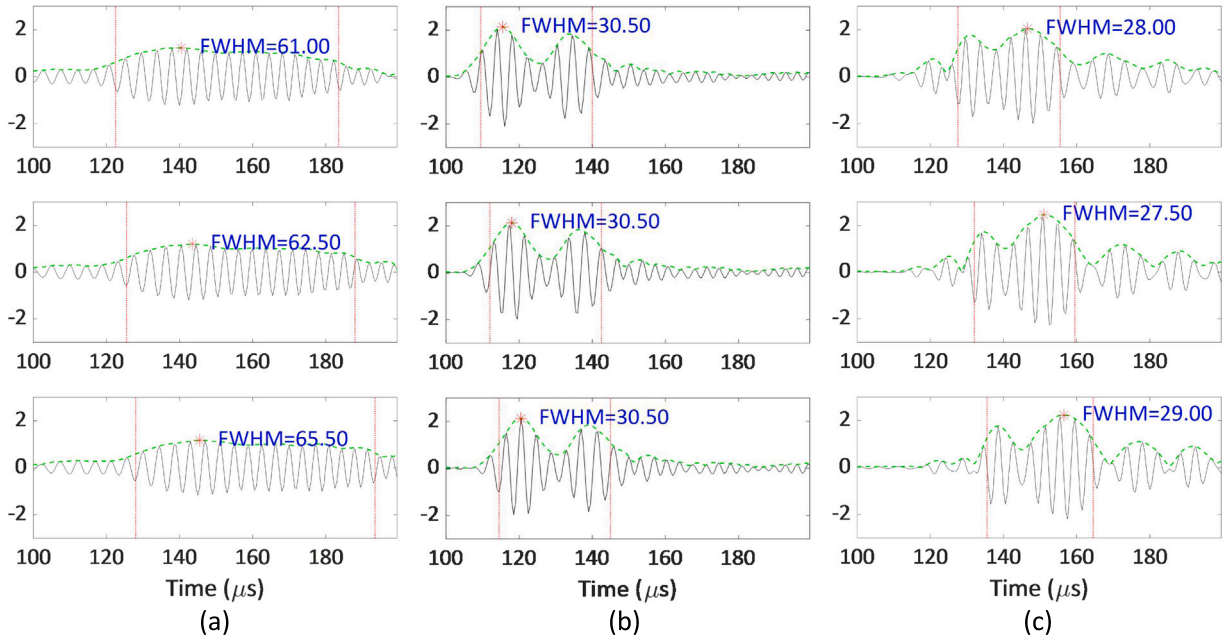

Fig. 9. Full width at half maximum (FWHM) of Hilbert envelopes computed from selected array sensors in a single propagation direction. (a) S_0 mode only. (b) A_0 mode only. (c) Combined $A0 + A1$ modal excitation. The $A0 + A1$ configuration yields the narrowest FWHM, indicating superior temporal resolution and validating the CRLB-based prediction of improved localization accuracy.

is performed. The scattered waveform received at a sensor can be locally approximated by a Gaussian envelope,

$$s(t) = A \exp\left[-\frac{(t-t_0)^2}{2\sigma_t^2}\right] \cos(\omega_0 t) \tag{33}$$

where σ_t characterizes the temporal width of the signal. For additive Gaussian noise of variance σ_n^2, the Fisher information with respect to the arrival time t_0 is

$$I(t_0) = \frac{1}{\sigma_n^2} \int_{-\infty}^{\infty} \left(\frac{\partial s(t)}{\partial t_0}\right)^2 dt \propto \frac{A^2}{\sigma_n^2 \sigma_t^2} \tag{34}$$

Thus the CRLB on the variance of any unbiased estimator of t_0 becomes

$$\mathrm{CRLB}(t_0) \propto \sigma_t^2 \tag{35}$$

The temporal FWHM of the signal is related to σ_t by

$$\mathrm{FWHM}_t = 2\sqrt{2\ln 2}\,\sigma_t \tag{36}$$

so that

$$\mathrm{CRLB}(t_0) \propto \mathrm{FWHM}_t^2 \tag{37}$$

Therefore, a narrower temporal FWHM corresponds to a larger Fisher information in arrival-time estimation, which directly improves the localization accuracy in TFM-based imaging. The observed reductions in temporal FWHM for combinations of A_0 and A_1 modes are thus consistent with the CRLB-predicted improvements in defect localization.

The extracted FWHM distributions are summarized in Fig. 9. As clearly evidenced in the plots, the $A_0 + A_1$ case consistently yields the narrowest wave packet envelopes, with FWHM values significantly smaller than those of either single mode alone. This enhancement is attributed to constructive modal interference, where the superposition of A_0 and A_1 waveforms leads to amplitude reinforcement and temporal compression of the wave packet. The reduced FWHM reflects increased Fisher information due to improved temporal localization, thereby validating the CRLB-based conclusion that multi-mode Lamb wave excitation can significantly enhance defect localization performance in ultrasonic NDT.

Building on the physical insight obtained from the Hilbert envelope analysis, we then proceed to full-field imaging using the TFM. The impact of mode selection on image sharpness and defect localization is quantitatively evaluated. To examine the frequency dependence of the imaging performance, TFM imaging results using the S_0, A_0, and combined $A_0 + A_1$ modes are presented at three nearby excitation frequencies: 250 kHz (Fig. 10), 260 kHz (Fig. 11), and 270 kHz (Fig. 12), respectively. Across all frequencies,

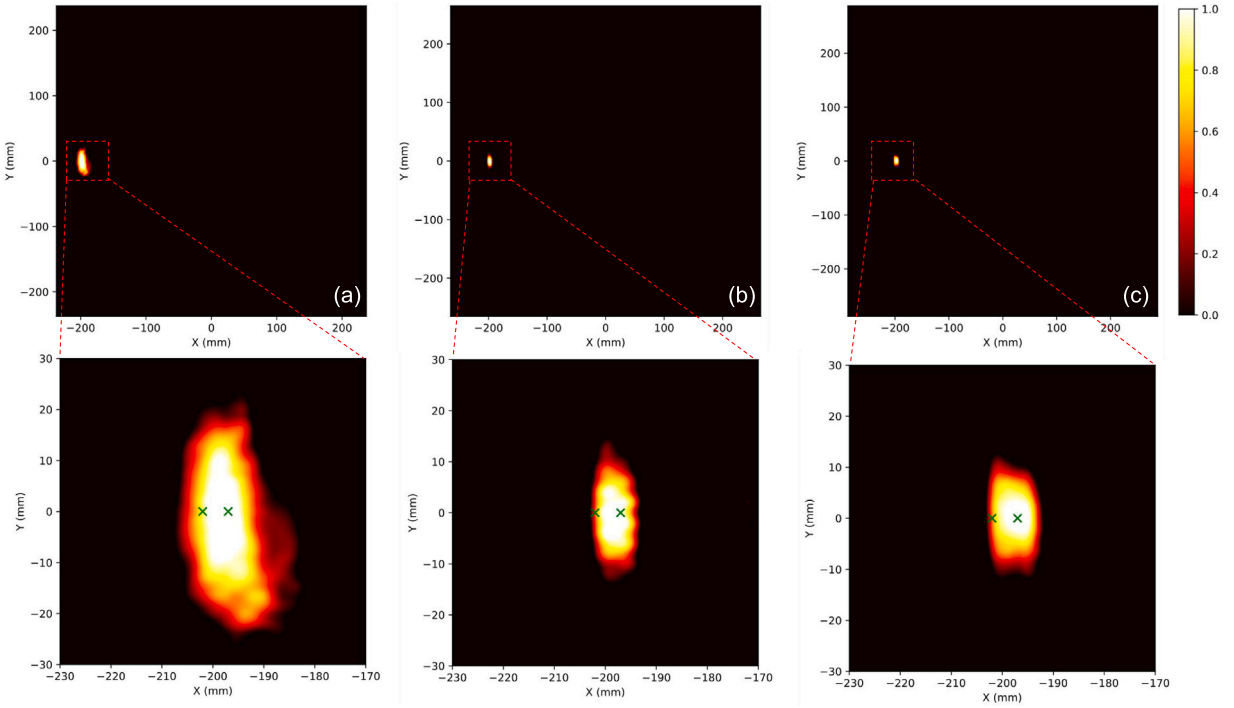

Fig. 10. TFM imaging results at 250 kHz using different Lamb wave modes. (a) S_0 mode imaging; (b) A_0-mode imaging; (c) Combined $A_0 + A_1$ imaging.

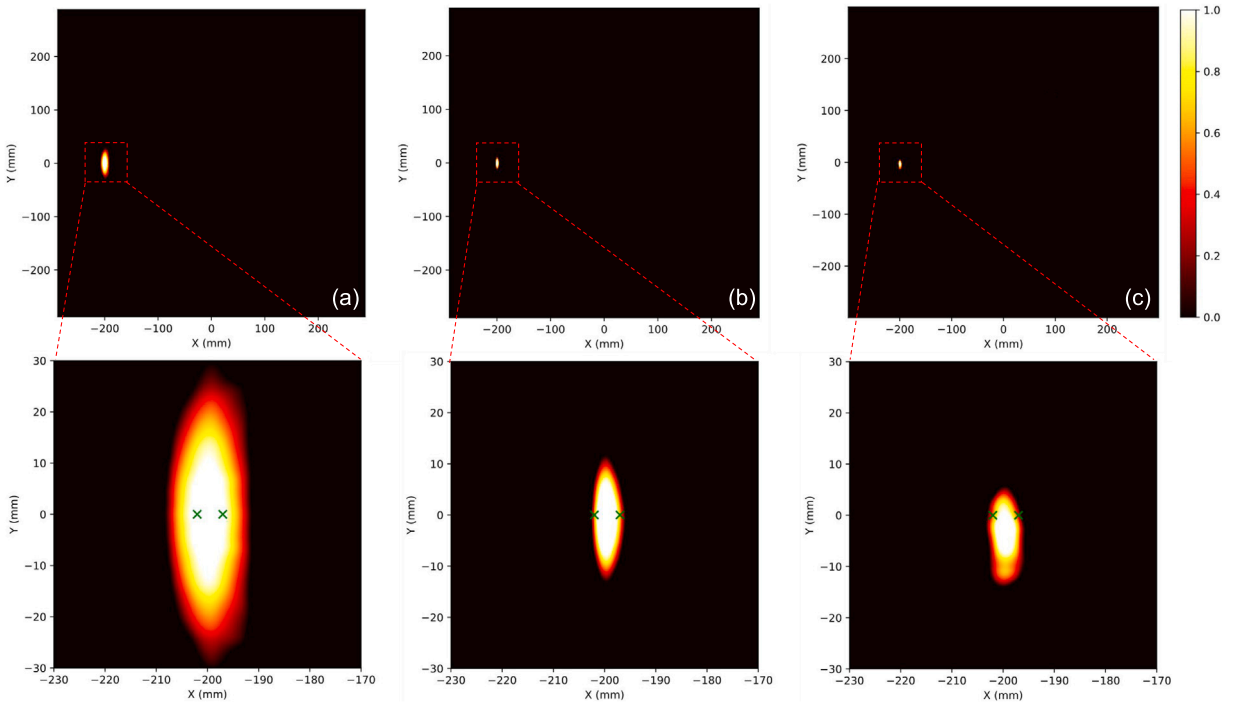

Fig. 11. TFM imaging results at 260 kHz using different Lamb wave modes. (a) S_0 mode imaging; (b) A_0-mode imaging; (c) Combined $A_0 + A_1$ imaging.

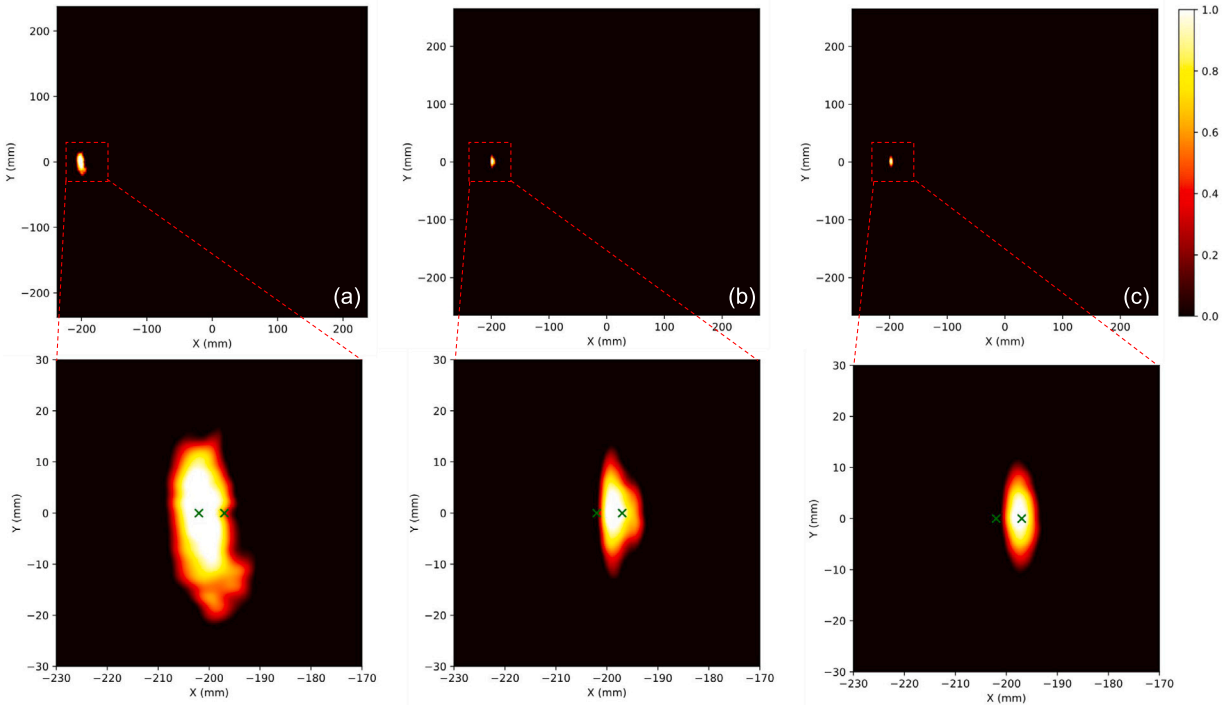

Fig. 12. TFM imaging results at 270 kHz using different Lamb wave modes. (a) S_0 mode imaging; (b) A_0-mode imaging; (c) Combined $A_0 + A_1$ imaging.

the combined $A_0 + A_1$ imaging consistently provides improved localization over the single-mode cases, indicating the robustness of the modal-diversity advantage. When analyzing the combined $A_0 + A_1$ excitation, we explicitly treat the two modes as incoherent components. This choice reflects the fact that A_0 and A_1 possess significantly different phase velocities and wavenumbers at 260 kHz, resulting in rapidly varying relative phases across the array that prevent stable inter-mode phase alignment. Accordingly, the total measured signal at receiver i is modeled as the superposition of two statistically independent modal contributions,

$$s_i(t) = s_i^{A_0}(t) + s_i^{A_1}(t) \tag{38}$$

and the FIM becomes the sum of the modal FIMs,

$$\mathbf{F} = \mathbf{F}_{A_0} + \mathbf{F}_{A_1} \tag{39}$$

To further examine the robustness of the multimodal formulation, the influence of the relative modal weighting on the localization uncertainty was investigated by varying the contribution of the A_1 mode while keeping the A_0 mode fixed. Fig. 13 illustrates the resulting CRLB for different relative A_0-A_1 weighting ratios. As expected, reducing the relative amplitude of the A_1 mode leads to a gradual increase in the CRLB, reflecting a reduced information contribution from this mode. Nevertheless, it is observed that for all considered weighting cases, the inclusion of the A_1 mode consistently yields a lower CRLB compared with the all-mode case. This behavior can be attributed to the intrinsically higher information density of the A_1 mode, which is associated with its shorter effective wavelength and enhanced phase sensitivity. As a result, even when the A_1 mode has a relatively small amplitude, it still contributes a disproportionally large amount of Fisher information per unit energy, leading to an overall improvement in localization precision. These results indicate that the adopted incoherent multimodal combination with different relative weights produces physically consistent and expected trends. The qualitative conclusion that higher-order modes enhance localization resolution therefore remains robust with respect to reasonable variations in relative modal amplitudes, as reflected by the corresponding CRLB predictions.

To ensure a physically meaningful comparison across modes, each modal waveform is normalized to have the same SNR before forming the combined signal. This avoids biasing the Fisher information toward the higher-energy mode and isolates the effect of modal dispersion on the CRLB. The resulting combined-mode CRLB therefore reflects the theoretical localization capability obtained when two independent modes of equal SNR contribute information to the array imaging process. It is observed that both the S_0 and A_0 modes exhibit inherent limitations in resolving the two circular hole defects, primarily constrained by the diffraction limit. However, imaging with the A_0 mode clearly outperforms the S_0 mode. This performance improvement is attributed to the A_0 mode's shorter wavelength and higher wavenumber, which translate to finer spatial resolution and lower localization uncertainty. Defect positions in the TFM images are extracted using a peak-based estimator. For each reconstructed TFM amplitude map, the defect

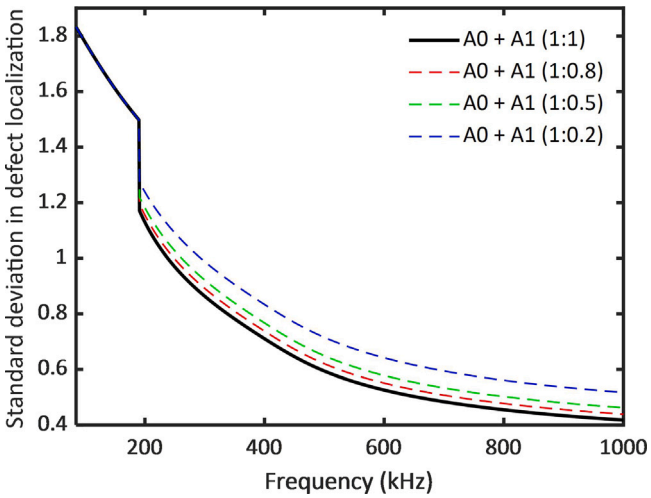

Fig. 13. CRLB of defect localization for different relative weighting ratios between the A_0 and A_1 Lamb wave modes under incoherent multimodal combination.

location is defined as the coordinate of the global maximum within a 10 × 10 mm neighborhood around the nominal defect region. This approach is consistent with the peak-based maximum likelihood (ML) estimator implicitly assumed in the CRLB formulation for point-like scatterers.

More notably, the integration of the A_1 mode alongside the A_0 mode results in a significant reduction in localization uncertainty, yielding the best imaging performance among all mode combinations considered. This improvement arises from the A_1 mode's heightened sensitivity to local thickness variations, which facilitates mode conversion into A_0 components with shorter wavelengths. The resulting modal synergy enhances sensitivity and spatial coherence, effectively lowering the CRLB and improving detectability. Although the diffraction limit fundamentally constrains resolution and cannot be surpassed without advanced algorithmic strategies, the multi-mode $A_0 + A_1$ approach leverages modal diversity to approach this limit more closely. This validates our theoretical CRLB formulation, indicating its effectiveness as a predictive tool for evaluating and optimizing mode-selective imaging strategies in Lamb wave-based NDT.

As discussed in Section 3.1, the achievable localization precision in TFM imaging is fundamentally governed by the Fisher information, which is proportional to the squared sensitivity of the received waveform to small perturbations in the propagation delay. This sensitivity is in turn strongly influenced by the effective frequency content and phase evolution of the propagating mode. For time-delay-based beamforming, a small spatial displacement of the defect induces a corresponding perturbation in the propagation delay, resulting in a phase shift of the received signal. The magnitude of this phase variation scales approximately with the effective angular frequency of the mode, implying that modes with higher effective frequencies (shorter equivalent wavelengths) provide larger signal gradients with respect to spatial coordinates. Consequently, these modes contribute higher Fisher information and yield tighter CRLBs, translating into improved spatial resolution in TFM imaging. In the present study, the A_1 mode exhibits a substantially higher effective frequency content compared with the fundamental A_0 and S_0 modes under the same excitation conditions. This interpretation is consistent with both the CRLB predictions and the numerical TFM imaging results.

To further quantify these observations, the imaging results are evaluated using two key metrics: the array performance indicator (API) and the transverse intensity curve (TIC), as illustrated in Fig. 14; detailed definitions and formulations of these metrics can be found in Appendix B. The API quantitatively reflects the array's effective spatial resolving capability, while the transverse intensity curve provides insight into the lateral distribution of image energy around the defect region. To convert the API/TIC imaging metrics into a form directly comparable with the CRLB, the localization error of each defect is extracted by performing the same 2D Gaussian peak fitting. For each modal configuration (A_0, S_0 and $A_0 + A_1$), the root-mean-square localization error σ_{TFM} across all array reconstructions is computed and compared to the theoretical CRLB value σ_{CRLB} predicted at the same SNR. A dimensionless efficiency ratio is defined,

$$\eta = \frac{\sigma_{\mathrm{TFM}}}{\sigma_{\mathrm{CRLB}}} \tag{40}$$

where $\eta = 1$ indicates that the TFM estimator attains the theoretical limit.

To more comprehensively assess the validity of the CRLB-based resolution framework under practical measurement conditions, additional TFM analyses are performed by systematically varying the SNR and the spatial sampling density (sensor spacing 10 mm), as illustrated in Fig. 15.

Table 1 summarizes the efficiency ratio $\eta = \sigma_{\mathrm{TFM}}/\sigma_{\mathrm{CRLB}}$ obtained from TFM imaging under different noise and spatial sampling conditions. For the single-mode A_0 and S_0 cases, the simulations are performed in a high-SNR regime (approximately 30 dB) with dense spatial sampling, providing a baseline for comparison. For the multimodal $A_0 + A_1$ configuration, both the sensor spacing

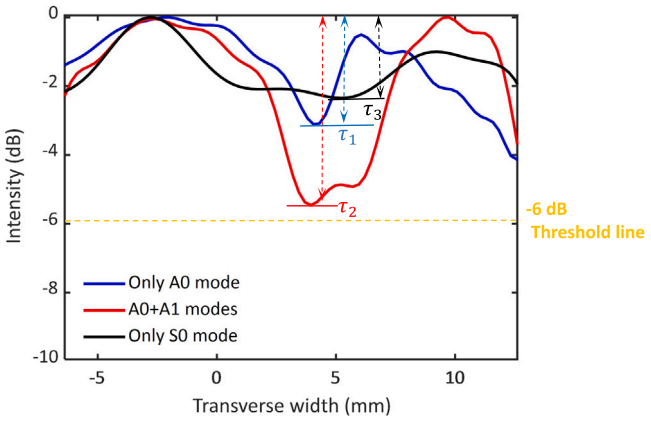

Fig. 14. Quantitative transverse intensity curves for different Lamb wave modes obtained from COMSOL simulations.

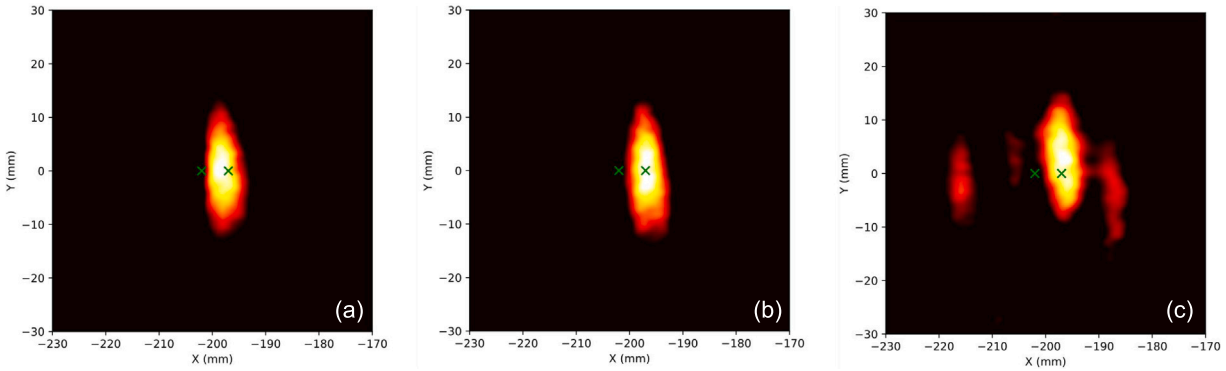

Fig. 15. TFM imaging results obtained for the $A_0 + A_1$ multimodal configuration with a fixed aperture size of 100 mm × 100 mm and a sensor spacing of 10 mm. The SNR is set to (a) 30 dB, (b) 20 dB, and (c) 10 dB, respectively. As the noise level increases, the image contrast and localization sharpness gradually degrade, as expected.

Table 1
Efficiency ratio $\eta = \sigma_{\mathrm{TFM}}/\sigma_{\mathrm{CRLB}}$ obtained from TFM imaging under different noise and spatial sampling conditions. The aperture size is fixed at 100 mm × 100 mm. Values close to unity indicate localization performance approaching the theoretical CRLB.

Modal configuration	SNR (dB)	Sensor spacing (mm)	η (simulation)
A_0 only	30	5	1.32 ± 0.08
S_0 only	30	5	1.48 ± 0.10
$A_0 + A_1$	30	5	1.11 ± 0.08
$A_0 + A_1$	30	10	1.14 ± 0.09
$A_0 + A_1$	20	10	1.20 ± 0.10
$A_0 + A_1$	10	10	1.31 ± 0.12

and noise level are systematically varied. Increasing the sensor spacing from 5 mm to 10 mm and reducing the SNR lead to a gradual increase in the efficiency ratio, reflecting the increased sensitivity of practical TFM localization to spatial undersampling and measurement noise. Despite these variations, the A_0+A_1 configuration consistently exhibits the lowest efficiency ratio among all considered cases. Even under a low-SNR condition of 10 dB, the localization error remains within approximately 30% of the CRLB. These results demonstrate that, although the numerical value of the efficiency ratio depends on implementation factors such as noise level and spatial sampling density, the qualitative conclusion regarding the near-optimal and robust localization performance of the multimodal $A_0 + A_1$ configuration remains unchanged.

4.1.2. Lateral separability analysis for practically relevant limited-view imaging

In the previous subsection, the axial two-target case was treated only as a controlled benchmark, as it facilitates the isolation of temporal waveform overlap, modal interference, and noise effects under the adopted envelope-based narrowband processing. To further address the practical relevance of limited-view guided-wave imaging, lateral target separability was additionally investigated

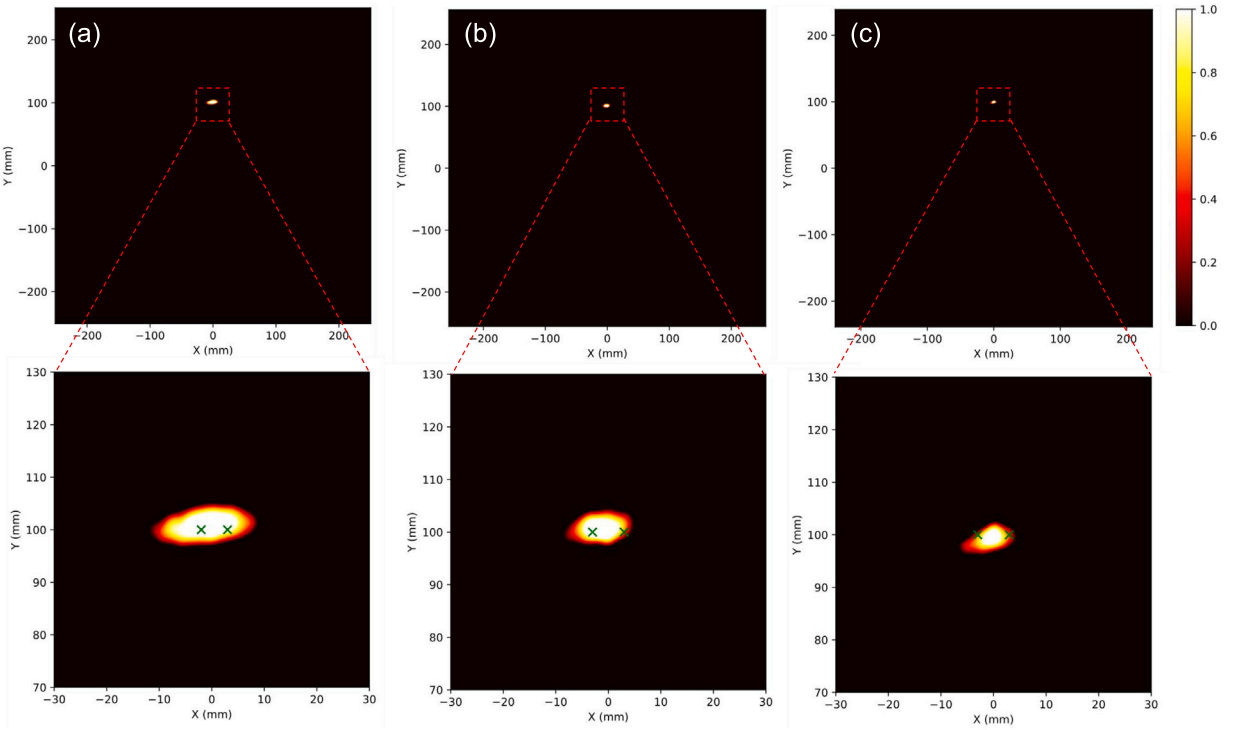

Fig. 16. FE TFM imaging results for two laterally separated point-like defects located at the same propagation range with a lateral spacing of 5 mm: (a) S_0 mode imaging; (b) A_0 mode imaging; (c) combined $A_0 + A_1$ imaging. The $A_0 + A_1$ configuration provides the most concentrated localization, indicating superior lateral separability.

using two point-like defects located at the same propagation range with a lateral spacing of 5 mm. This spacing was selected as a representative lateral case, consistent with the sub-diffraction setting adopted throughout the present study. Because both defects are placed at the same propagation range, the present configuration avoids the front–back masking inherent to the axial benchmark and enables the practically relevant separability limit to be examined directly along the lateral direction.

To express the lateral counterpart of the axial benchmark within the same reduced-Fisher-information framework, the CRLB-predicted uncertainty of the lateral spacing $\Delta x = x_2 - x_1$ is written as

$$\sigma_{\Delta x} = \sqrt{\mathbf{a}_{\mathrm{lat}}^{\top}\mathbf{J}_{\mathrm{red}}^{-1}\mathbf{a}_{\mathrm{lat}}}, \qquad \mathbf{a}_{\mathrm{lat}} = [-1,\ 0,\ 1,\ 0]^{\top} \tag{41}$$

where $\mathbf{J}_{\mathrm{red}}$ denotes the reduced Fisher information matrix after elimination of nuisance parameters. In contrast to the axial case, Eq. (41) explicitly projects the localization uncertainty onto the lateral separation coordinate at a common propagation range.

The corresponding TFM reconstructions obtained using the S_0 mode, the A_0 mode, and the combined $A_0 + A_1$ configuration are presented in Fig. 16(a)–(c), respectively. The S_0-based image exhibits the broadest and most overlapped response, indicating limited lateral discrimination capability. When the A_0 mode is used, the focal response becomes narrower, reflecting the improved spatial sensitivity associated with its shorter wavelength. Among the three cases, the $A_0 + A_1$ image provides the most concentrated localization and the clearest separation tendency, demonstrating that the multimodal antisymmetric combination offers the best lateral separability under the adopted envelope-based TFM formulation.

These observations are consistent with the CRLB-based interpretation developed in the preceding sections: higher-information modal combinations lead to reduced localization uncertainty and improved practical separability. The present lateral example therefore provides a more practically relevant validation of the proposed framework for limited-view guided-wave imaging and shows that the CRLB-based interpretation remains consistent when the separability problem is considered along the lateral axis.

4.2. Experimental validations

For laboratory experimental validation, two T6061 aluminum plates (1000 mm × 1000 mm × 8 mm) are prepared as test samples, as illustrated in Fig. 17. To examine the applicability of the proposed framework under different defect orientations, two crack-like defects with distinct spatial configurations are introduced. In the first specimen, a crack-like defect is positioned along the propagation (axial) direction, located 200 mm to the left of the plate center, corresponding to the axial defect configuration adopted in the numerical study. In the second specimen, a crack-like defect is placed along the transverse (lateral) direction, located 100 mm

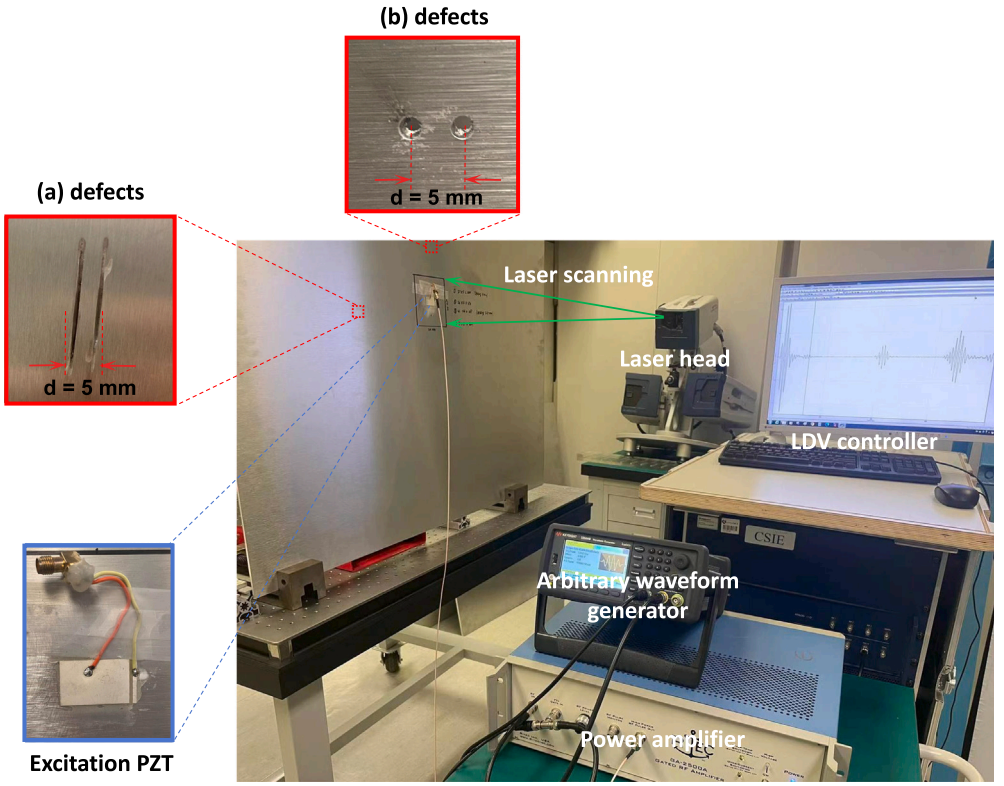

Fig. 17. The experimental setup entailed the collection of ultrasonic Lamb wave signals, with a specific focus on a designated region of interest within the tested aluminum plate.

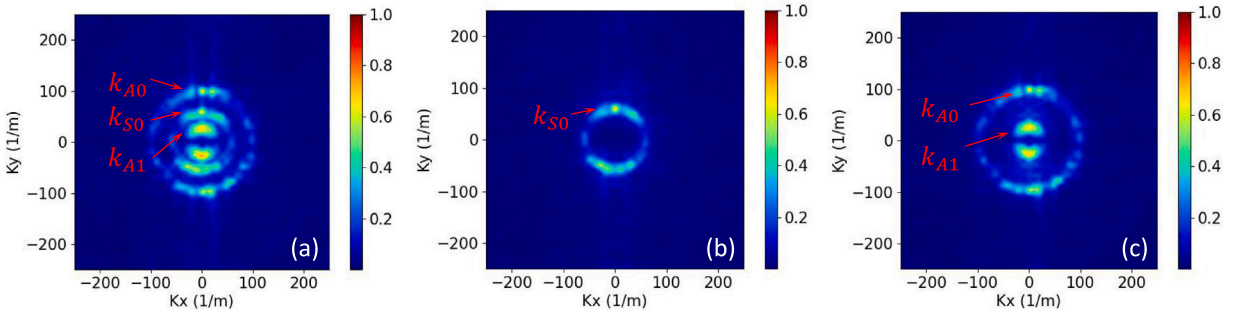

Fig. 18. Wavenumber spectrograms for (a) all modes, (b) S_0 mode only and (c) antisymmetric modes.

above the plate center. These two experimental configurations are designed to respectively represent a controlled axial localization scenario and a more realistic lateral defect orientation commonly encountered in guided-wave NDT inspections.

To initiate the experiment, we apply a 5-cycle Hanning window sinusoidal signal with a frequency of 260 kHz, PZTs were symmetrically mounted on both sides of the plate to facilitate the excitation of antisymmetric and symmetric modes. Simultaneously, we conduct out-of-plane displacement scanning in the region of interest with a sampling frequency of 5.12 MHz, using a Polytec PSV Qtec 3D PSV500 system. The recorded displacement reflects the surface response of the plate induced by the propagation of guided Lamb waves. The wavenumber spectrograms (Fig. 18) confirm the excitation of the A_1 mode, demonstrating that our experiment successfully achieves mode-selective actuation.

Building upon the mode identification, we quantitatively evaluated the temporal localization characteristics of each mode by extracting their Hilbert envelopes and computing the FWHM across selected array channels. As illustrated in Fig. 19, the combined A_0+A_1 excitation consistently exhibits the narrowest FWHM, indicating superior wave packet compression and enhanced resolution compared to single-mode excitations. This experimentally observed trend is consistent with our earlier finite element analysis, thereby reinforcing the robustness of the finding across both simulation and measurement. The result validates that the $A_0 + A_1$

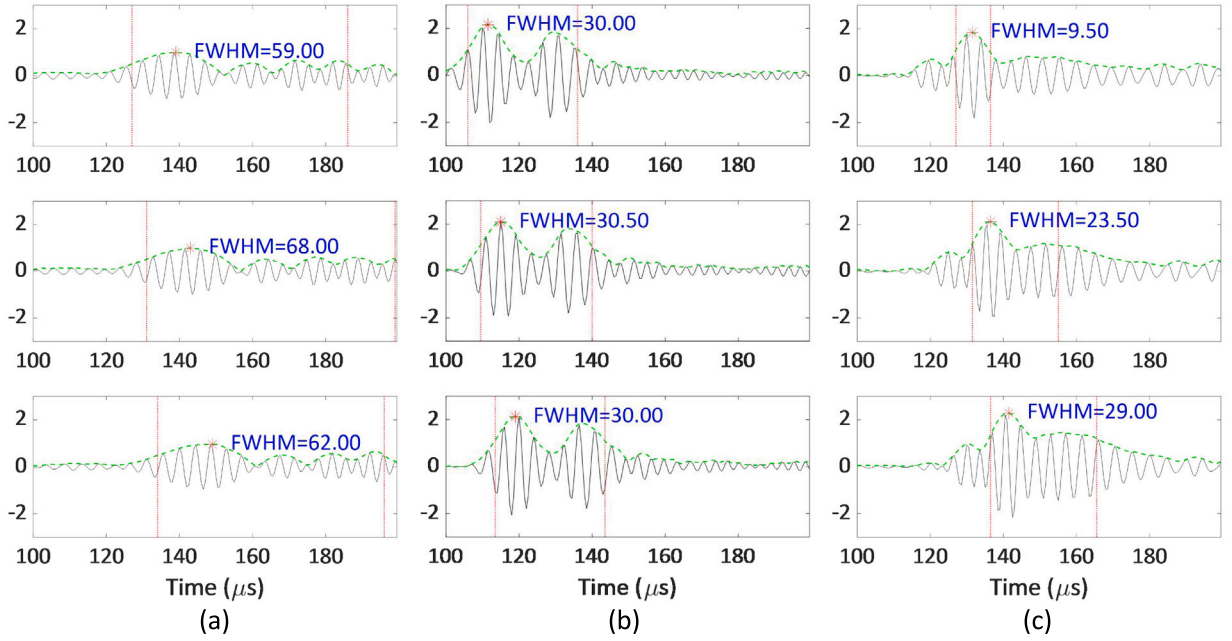

Fig. 19. Full width at half maximum (FWHM) of Hilbert envelopes computed from selected array sensors in a single propagation direction. (a) S_0 mode only. (b) A_0 mode only. (c) Combined $A_0 + A_1$ modal excitation. The $A_0 + A_1$ configuration yields the narrowest FWHM, indicating superior temporal resolution and validating the CRLB-based prediction of improved localization accuracy.

Table 2
Experimental efficiency ratio $\eta = \sigma_{\mathrm{TFM}}/\sigma_{\mathrm{CRLB}}$ computed from repeated measurements on the aluminum plate. Experimental trends are consistent with simulations, with the $A_0 + A_1$ configuration achieving the closest approach to the CRLB.

Modal configuration	η (experiment)
A_0 only	1.41 ± 0.12
S_0 only	1.56 ± 0.15
$A_0 + A_1$	1.18 ± 0.07

configuration benefits from constructive modal interference, which compresses the wave packet duration, reduces localization uncertainty, increases the Fisher information, and consequently lowers the CRLB for defect position estimation.

Subsequently, the separated mode datasets are employed for TFM imaging. For the axial defect configuration, the reconstructed images corresponding to the S_0, A_0, and $A_0 + A_1$ modes are presented in Fig. 20, allowing a direct comparison of their defect localization performance. Similarly, the TFM results for the lateral defect configuration are shown in Fig. 21. This consistent behavior across axial and lateral defect configurations indicates that the enhanced spatial resolution achieved by multimodal combination is not restricted to a specific defect orientation, and further supports the robustness of the proposed framework. Notably, the $A_0 + A_1$ result yields the most concentrated focal spot with reduced sidelobe energy, indicating that constructive mode interference may enhance spatial resolution of array imaging. This resolution enhancement is further validated by the transverse intensity profiles (Fig. 22). A similar efficiency analysis is performed for the experimental measurements. Table 2 summarizes the experimentally obtained values of η, showing the same ordering as the numerical simulations: the $A_0 + A_1$ configuration yields the smallest ratio and therefore operates closest to the CRLB. Although the experimental ratios are slightly larger due to instrumental noise and coupling variability, the overall agreement with the simulation-based trend indicates that the proposed modal strategy consistently improves the estimator efficiency in both simulated and real measurements.

These observations collectively validates that antisymmetric modes, particularly the A_1 mode, play a critical role in achieving high-resolution array imaging. Their stronger interaction with structural anomalies, combined with a lower CRLB for localization accuracy, makes them effective for defect detection. In other words, these modes are associated with smaller theoretical limits on the variance of position estimates, leading to more precise localization. Overall the laboratory experiments indicate that *informed* mode selection by the established quantitative framework, may push TFM imaging performance closer to the theoretical limit, enhancing its potential for more accurate and reliable ultrasonic NDT.

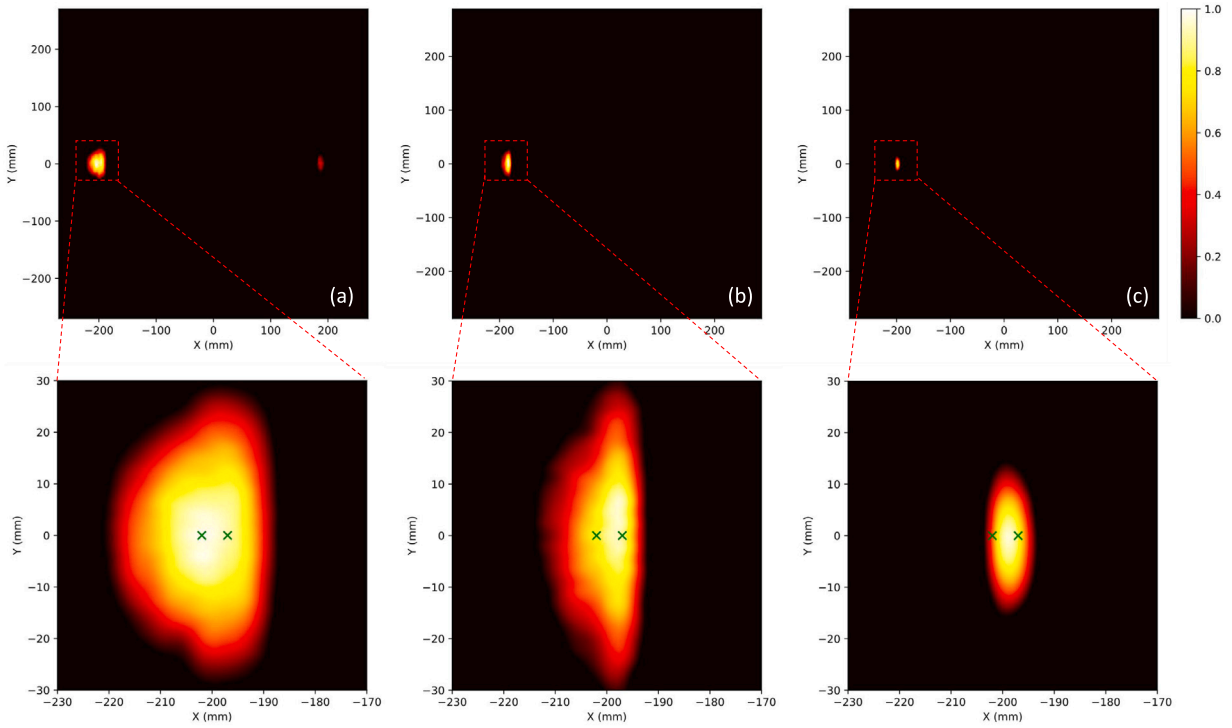

Fig. 20. The defect is located 200 mm from the plate center along the propagation (axial) direction.
TFM results using different Lamb wave modes in experimental validation of sub-wavelength defect detection: (a) Using only the S_0 mode, (b) Using only the A_0 mode and (c) Using antisymmetric modes ($A_0 + A_1$).

5. Conclusion

This work develops a CRLB-based statistical framework for interpreting localization uncertainty in classical envelope-based Lamb-wave TFM. The framework provides a transparent and model-conditioned benchmark for examining how wavelength, aperture, and modal content influence diffraction-related localization behavior.

The critical impact of multi-modal Lamb wave on the diffraction limit is particularly studied and quantified by the indicated CRLB-based resolution analysis framework. The inclusion of higher-order modes enriches the FIM, thereby lowering the CRLB and reducing localization uncertainty. In particular, the antisymmetric A_1 mode exhibits pronounced advantages owing to its strong dispersive characteristics, high sensitivity to structural discontinuities, and the generation of mode-converted components with shorter effective wavelengths. These features collectively enable enhanced resolution and further reductions in CRLB, especially when antisymmetric modes are selectively exploited. Experimental validation through LDV scanning further validates that mode-selective imaging, especially with combined A_0 and A_1 modes, approaches the CRLB-predicted limits and outperforms conventional mode strategies by enhancing spatial resolution within the TFM beamforming framework through selective exploitation of antisymmetric modes. In the present study, the analysis is intentionally focused on classical time-delay-based DAS/TFM formulations, which remain widely adopted in guided-wave NDT and provide a transparent and interpretable benchmark for linking diffraction-induced point spread behavior with estimator performance. Extending the CRLB-based analysis to alternative beamforming formulations, including phase-consistent or dispersion-aware implementations, may offer additional perspectives on estimator behavior within the same information-theoretic framework, and is therefore identified as a potential direction for future investigation.

By integrating CRLB theory with practical Lamb wave array imaging and quantitatively linking it to the diffraction limit, this work, overall, contributes to the advances in the theoretical foundation of resolution analysis in ultrasonic array imaging for NDT. Building upon this basis, it may inspire one, in future research, to develop quantifiable *super-resolution* techniques and advanced mode-aware imaging algorithms that work around such an imaging resolution limit for more precise and reliable ultrasonic array defect characterization in complex structures. Moreover, as the LDV measurements operate under a fixed instrumental and environmental noise floor, the experimental SNR cannot be systematically varied without compromising repeatability; therefore, the experiment validates the CRLB analysis under realistic laboratory noise conditions. A more comprehensive multi-noise-level validation should be explored in future work.

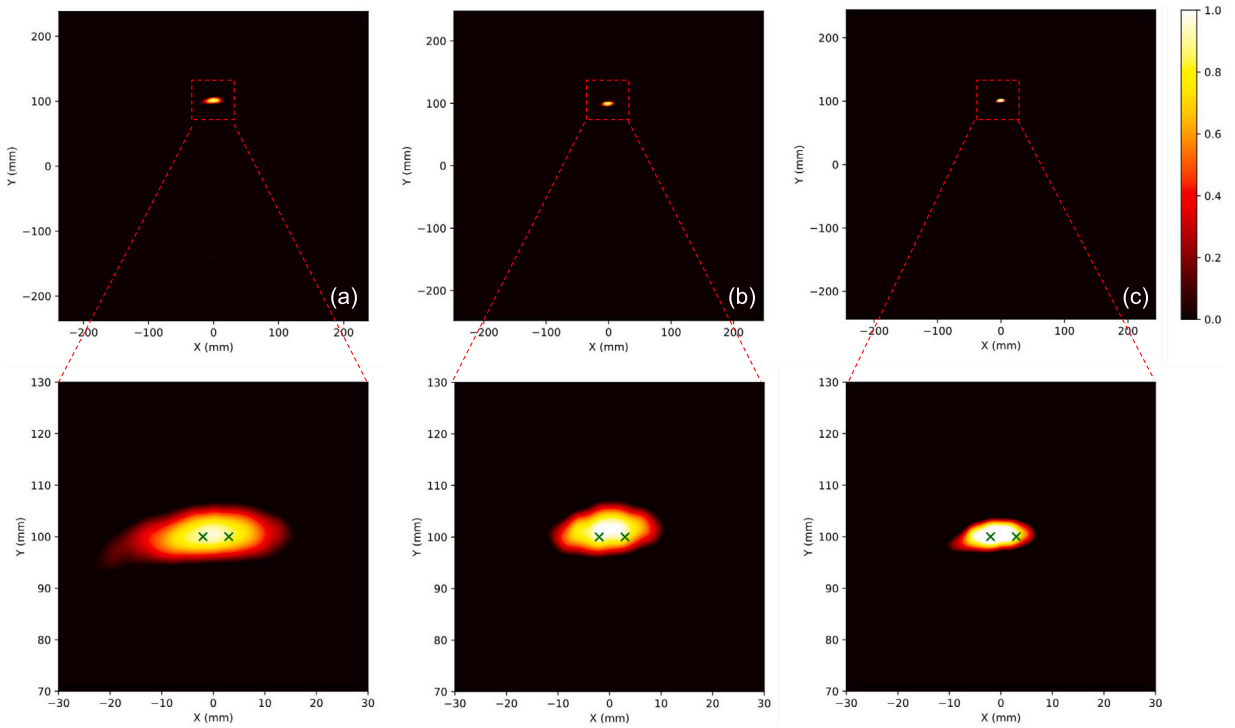

Fig. 21. The defect is located 100 mm above the plate center along the transverse (lateral) direction. TFM results using different Lamb wave modes in experimental validation of sub-wavelength defect detection: (a) Using only the S_0 mode, (b) Using only the A_0 mode and (c) Using antisymmetric modes ($A_0 + A_1$).

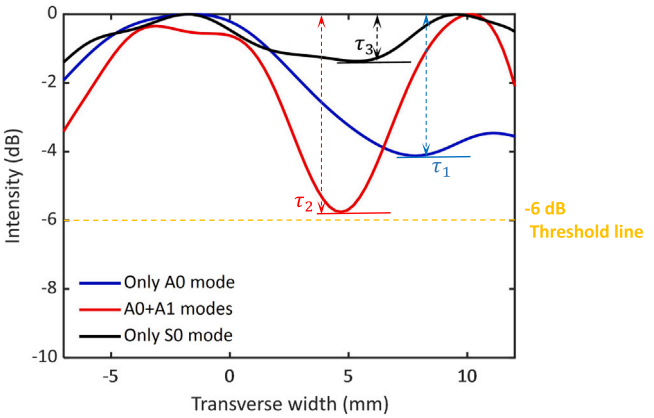

Fig. 22. Quantitative transverse intensity curves for different Lamb wave modes obtained from experimental measurements.

CRediT authorship contribution statement

Tingjian Li: Writing – original draft, Validation, Software, Methodology, Investigation. **Shanwu Li:** Writing – review & editing, Validation, Methodology, Investigation. **Shengbo Shan:** Validation, Resources, Investigation. **Li Cheng:** Writing – review & editing, Supervision, Resources, Methodology, Investigation. **Yongchao Yang:** Writing – review & editing, Supervision, Resources, Project administration, Methodology, Investigation, Funding acquisition, Conceptualization.

Financial disclosure

None reported.

Declaration of competing interest

The authors declare that they have no known competing financial interests or personal relationships that could have appeared to influence the work reported in this paper.

Acknowledgments

The research was partially funded by the National Key Research and Development Program of China (Grant No. 2024YFC3808604), the National Natural Science Foundation of China (Grant No. 52478315), and the Key Program of the Natural Science Foundation of Zhejiang (Grant No. LZ25E080001).

Appendix A. Derivation of the CRLB expression based on lamb wave measurement models

Note that in this study we need to calculate the phase φ_{ij} of each receiver. When the defect's position (x_0, y_0) aligns with the focal point, the array element i experiences a time delay, denoted as t_{di} relative to the focal distance R, as shown in Fig. 1. The distance between defect and the array element with sequence number i at the coordinate origin o is r, the deflection angle of the defect is θ_d. This delay is computed using Eq. (A.1):

$$t_i = \frac{\sqrt{\left(x_0 - y_0\right)^2} + \sqrt{\left(x_i - x_0\right)^2 + \left(y_i - y_0\right)^2}}{c_g} \tag{A.1}$$

$$t_i \approx t_{di} = t|_{\theta_d = \theta_i} = \frac{\sqrt{R^2 + {x_i}^2 + {y_i}^2 - 2Rx_i y_i \cos\left(\frac{\pi}{2} - \theta_0\right)}}{c_g} \tag{A.2}$$

By further simplifying time delay t_{di}, in relation to the defect

$$t_{di} \approx \frac{1}{c_g}\left(R + \frac{{x_i}^2}{2R} + \frac{{y_i}^2}{2R} - x_i y_i \sin\left(\theta_0\right)\right) \tag{A.3}$$

Subsequently, after applying a focus delay to array element i, the phase φ_i of the defect's location P in the range index l is expressed as follows:

$$\varphi_i(l) = wlT + w\left(t_{di} - t_i\right) = wlT + \frac{wx_i}{c_g}\left(\sin\theta_i - \sin\theta_0\right) \tag{A.4}$$

where ω is the angular frequency, T the sampling period, and l the range index. Considering Eq. (A.2), where ωlT is the dominant factor unaffected by the array element for a specific range index l and is thus disregarded. Then the phase φ_i of the received signal at the array sensor element $1 \le i \le N$ is

$$\varphi_i(l) = \frac{wx_i}{c_g}\left(\sin\theta_i - \sin\theta_0\right) \tag{A.5}$$

Given that the phase φ_i of the scattered signal exhibits a linear variation with the location x_i of the array elements, it is observed that all signals share the same polarity when the absolute value of the phase difference between the array elements reaches its maximum $|\varphi_N - \varphi_1| \le \pi$. Thus [26],

$$\left|\frac{2\pi}{\lambda}\left(x_N - x_1\right)\left(\sin\theta_i - \sin\theta_0\right)\right| \le \pi \tag{A.6}$$

where $(x_N - x_1) = D$, and D is the aperture size, then Eq. (A.6) is expressed as

$$\left|\sin\theta_i - \sin\theta_0\right| \le \frac{\lambda}{2D} \tag{A.7}$$

in Eq. (A.7), defining which all signals can be considered strictly coherent, when $\theta_i \approx \theta_0 = \theta_{coherent}$, then above Eq. (A.7) is represented as follows.

$$\left|\left(\sin\theta_i - \sin\theta_0\right)\right| \approx 2\cos\theta_0 \left|\sin\frac{\theta_{coherent} - \theta_0}{2}\right| = \frac{\lambda}{2D} \tag{A.8}$$

substitution of Eq. (A.8) into Eq. (A.5),

$$\varphi_i = \frac{2\pi x_i}{\lambda}\frac{\lambda}{2D} = \frac{\pi x_i}{D} \tag{A.9}$$

It is seen that phase φ_i is related to the ratio of the sensor's position to the aperture size.

The amplitudeA_j of each mode is obtained through mode separation techniques applied to individual Lamb wave components, though a detailed discussion of this process is beyond the scope of this work. Once both phase φ_i and amplitude A_j information are available, they are incorporated into the CRLB formulation to compute the theoretical bounds of parameter estimation.

Appendix B. Resolution and performance analysis of TFM imaging based on quantitative indicators

To rigorously quantify the effectiveness of the TFM imaging, the peak to center intensity difference and the array performance indicator (API) [51] are used. First, the performance of TFM imaging in distinguishing two adjacent defects is quantified using the peak to center intensity difference, denoted as τ. It follows the −6 dB drop method and serves as a measure for evaluating the algorithm's capability to resolve and differentiate between the two targets. Furthermore, it interprets the correlation between ultrasonic imaging and the diffraction limit. If a specific threshold is exceeded, for example, $\tau \leq -6$ dB, the two scatterers are typically deemed resolved. Conversely, if $\tau > -6$ dB, the two scatterers cannot be distinguished from each other.

Another one, the Array Performance Indicator (API), is used to quantify the size of the image(s) of the target(s). It is defined as follows [51]:

$$\mathrm{API} = \frac{\mathrm{Area}_{-6\mathrm{dB}}}{\lambda^2} \tag{B.1}$$

where $\mathrm{Area}_{-6\mathrm{dB}}$ represents the region of the image where the amplitude exceeds −6 dB above its maximum value within the designated imaging area.

For further quantification, the Transverse Intensity Curve is used to assess the lateral resolution and the characteristics of the Point Spread Function (PSF). It is a tool used to describe the lateral resolution of an imaging system by analyzing the width of the PSF, thus illustrating the resolving capacity of the system.

Data availability

Data will be made available on request.

References

[1] V. Giurgiutiu, J. Bao, Embedded-ultrasonics structural radar for in situ structural health monitoring of thin-wall structures, Struct. Health Monit. 3 (2) (2004) 121–140.
[2] Z. Su, L. Ye, Y. Lu, Guided lamb waves for identification of damage in composite structures: A review, J. Sound Vib. 295 (3–5) (2006) 753–780.
[3] F. Chen, P.D. Wilcox, The effect of load on guided wave propagation, Ultrasonics 47 (1–4) (2007) 111–122.
[4] R. Guan, Y. Lu, K. Wang, Z. Su, Fatigue crack detection in pipes with multiple mode nonlinear guided waves, Struct. Health Monit. 18 (1) (2019) 180–192.
[5] V. Giurgiutiu, Structural Health Monitoring: with Piezoelectric Wafer Active Sensors, Elsevier, 2007.
[6] S. Shan, J. Qiu, C. Zhang, H. Ji, L. Cheng, Multi-damage localization on large complex structures through an extended delay-and-sum based method, Struct. Health Monit. 15 (1) (2016) 50–64.
[7] Z. Liu, J. Fan, Y. Hu, C. He, B. Wu, Torsional mode magnetostrictive patch transducer array employing a modified planar solenoid array coil for pipe inspection, Ndt & E Int. 69 (2015) 9–15.
[8] Z. Liu, K. Sun, G. Song, C. He, B. Wu, Damage localization in aluminum plate with compact rectangular phased piezoelectric transducer array, Mech. Syst. Signal Process. 70 (2016) 625–636.
[9] L. Yu, Z. Tian, C.A. Leckey, Crack imaging and quantification in aluminum plates with guided wave wavenumber analysis methods, Ultrasonics 62 (2015) 203–212.
[10] L. Pahlavan, G. Blacquière, Fatigue crack sizing in steel bridge decks using ultrasonic guided waves, Ndt & E Int. 77 (2016) 49–62.
[11] L. Yu, Z. Tian, Guided wave phased array beamforming and imaging in composite plates, Ultrasonics 68 (2016) 43–53.
[12] Z. Tian, L. Yu, C. Leckey, Delamination detection and quantification on laminated composite structures with lamb waves and wavenumber analysis, J. Intell. Mater. Syst. Struct. 26 (13) (2015) 1723–1738.
[13] B.W. Drinkwater, P.D. Wilcox, Ultrasonic arrays for non-destructive evaluation: A review, NDT E Int. 39 (7) (2006) 525–541.
[14] C. Fan, M. Caleap, M. Pan, B.W. Drinkwater, A comparison between ultrasonic array beamforming and super resolution imaging algorithms for non-destructive evaluation, Ultrasonics 54 (7) (2014) 1842–1850.
[15] H. Choi, J.S. Popovics, NDE application of ultrasonic tomography to a full-scale concrete structure, IEEE Trans. Ultrason. Ferroelectr. Freq. Control 62 (6) (2015) 1076–1085.
[16] E.B. Flynn, S.Y. Chong, G.J. Jarmer, J.-R. Lee, Structural imaging through local wavenumber estimation of guided waves, Ndt E Int. 59 (2013) 1–10.
[17] E.B. Flynn, N.D. Stull, Toward utilizing full-field laser-ultrasound for practical nondestructive inspection with acoustic wavenumber spectroscopy, in: 2018 IEEE International Ultrasonics Symposium, IUS, IEEE, 2018, pp. 1–7.
[18] W. Wang, H. Zhang, J.P. Lynch, C.E. Cesnik, H. Li, Experimental and numerical validation of guided wave phased arrays integrated within standard data acquisition systems for structural health monitoring, Struct. Control. Health Monit. 25 (6) (2018) e2171.
[19] J.E. Michaels, Ultrasonic wavefield imaging: Research tool or emerging NDE method? in: AIP Conference Proceedings, 1806, (1) AIP Publishing, 2017.
[20] X. Wang, M. Lin, J. Li, J. Tong, X. Huang, L. Liang, Z. Fan, Y. Liu, Ultrasonic guided wave imaging with deep learning: Applications in corrosion mapping, Mech. Syst. Signal Process. 169 (2022) 108761.
[21] H. Song, Y. Yang, Accelerated noncontact guided wave array imaging via sparse array data reconstruction, Ultrasonics 121 (2022) 106672.
[22] Z. Tian, L. Yu, C. Leckey, Rapid guided wave delamination detection and quantification in composites using global-local sensing, Smart Mater. Struct. 25 (8) (2016) 085042.
[23] Z. Tian, S. Howden, Z. Ma, W. Xiao, L. Yu, Pulsed laser-scanning laser Doppler vibrometer (PL-SLDV) phased arrays for damage detection in aluminum plates, Mech. Syst. Signal Process. 121 (2019) 158–170.
[24] M. Sutcliffe, M. Weston, B. Dutton, P. Charlton, K. Donne, Real-time full matrix capture for ultrasonic non-destructive testing with acceleration of post-processing through graphic hardware, Ndt & E Int. 51 (2012) 16–23.
[25] H. Song, Y. Yang, Noncontact super-resolution guided wave array imaging of subwavelength defects using a multiscale deep learning approach, Struct. Health Monit. 20 (4) (2021) 1904–1923.
[26] W. Zhu, Y. Xiang, H. Zhang, M. Zhang, G. Fan, H. Zhang, Super-resolution ultrasonic lamb wave imaging based on sign coherence factor and total focusing method, Mech. Syst. Signal Process. 190 (2023) 110121.
[27] H. Song, Y. Yang, Uncertainty quantification in super-resolution guided wave array imaging using a variational Bayesian deep learning approach, NDT & E Int. 133 (2023) 102753.

[28] J. Camacho, D. Atehortua, J. Cruza, J. Brizuela, J. Ealo, Ultrasonic crack evaluation by phase coherence processing and TFM and its application to online monitoring in fatigue tests, Ndt & E Int. 93 (2018) 164–174.
[29] C. Xu, M. Deng, Waveform correlation factor (WCF) weighted TFM imaging for lamb wave phased array, NDT & E Int. 129 (2022) 102647.
[30] L.P. Piedade, G. Painchaud-April, A. Le Duff, P. Bélanger, Compressive sensing strategy on sparse array to accelerate ultrasonic TFM imaging, IEEE Trans. Ultrason. Ferroelectr. Freq. Control 70 (6) (2023) 538–550.
[31] X. Wang, J. Li, D. Wang, X. Huang, L. Liang, Z. Tang, Z. Fan, Y. Liu, Sparse ultrasonic guided wave imaging with compressive sensing and deep learning, Mech. Syst. Signal Process. 178 (2022) 109346.
[32] D. Wang, X. Wang, S. Chen, J. Li, L. Liang, Y. Liu, Joint learning of sparse and limited-view guided waves signals for feature reconstruction and imaging, Ultrasonics 137 (2024) 107200.
[33] H. Song, Y. Yang, Super-resolution visualization of subwavelength defects via deep learning-enhanced ultrasonic beamforming: A proof-of-principle study, NDT & E Int. 116 (2020) 102344.
[34] W. Zhang, X. Chai, W. Zhu, S. Zheng, G. Fan, Z. Li, H. Zhang, H. Zhang, Super-resolution reconstruction of ultrasonic lamb wave TFM image via deep learning, Meas. Sci. Technol. 34 (5) (2023) 055406.
[35] S. Cantero-Chinchilla, P.D. Wilcox, A.J. Croxford, A deep learning based methodology for artefact identification and suppression with application to ultrasonic images, NDT & E Int. 126 (2022) 102575.
[36] L. Lin, J. Xiao, D. Zhang, J. Liao, Z. Ma, Fast and high-resolution ultrasonic sparse TFM imaging based on cyclesr, Mech. Syst. Signal Process. 236 (2025) 113030.
[37] C. Willberg, S. Duczek, J.V. Perez, D. Schmicker, U. Gabbert, Comparison of different higher order finite element schemes for the simulation of lamb waves, Comput. Methods Appl. Mech. Engrg. 241 (2012) 246–261.
[38] A. De Miguel, A. Pagani, E. Carrera, Higher-order structural theories for transient analysis of multi-mode lamb waves with applications to damage detection, J. Sound Vib. 457 (2019) 139–155.
[39] D. Cirtautas, V. Samaitis, L. Mažeika, R. Raišutis, E. Žukauskas, Selection of higher order lamb wave mode for assessment of pipeline corrosion, Metals 12 (3) (2022) 503.
[40] C.H. Wang, J.T. Rose, F.-K. Chang, A synthetic time-reversal imaging method for structural health monitoring, Smart Mater. Struct. 13 (2) (2004) 415.
[41] H. Cramér, Mathematical methods of statistics, vol. 26, Princeton University Press, 1999.
[42] N. Stull, M. Mascarenas, E.B. Flynn, On performance limits in estimating thickness of a plate-like structure from a full-field single-tone response lamb wave measurement, in: 11th International Workshop on Structural Health Monitoring 2017: Real-Time Material State Awareness and Data-Driven Safety Assurance, IWSHM 2017, Unknown Publisher, 2017, pp. 1739–1746.
[43] N. Stull, E. Flynn, M. Mascarenas, On the theoretical limitations in estimating thickness of a plate-like structure from a full-field single-tone response lamb wave measurement, Ultrasonics 108 (2020) 106230.
[44] S. Li, F.A. Azad, Y. Yang, On the fundamental sensitivity limit of incoherent optical methods for full-field displacement measurements, IEEE Trans. Instrum. Meas. 72 (2023) 1–4, http://dx.doi.org/10.1109/TIM.2023.3311056.
[45] A. Perelli, L. De Marchi, A. Marzani, N. Speciale, Frequency warped cross-wavelet multiresolution analysis of guided waves for impact localization, Signal Process. 96 (2014) 51–62.
[46] J.M. Nichols, M.N. Hutchinson, N. Menkart, G.A. Cranch, G.K. Rohde, Time delay estimation via wasserstein distance minimization, IEEE Signal Process. Lett. 26 (6) (2019) 908–912.
[47] Y. Liu, W. Qi, S. Zhang, Z. Wang, A phase-based ranging method for fast frequency hopping system, in: 2014 Sixth International Conference on Wireless Communications and Signal Processing, WCSP, IEEE, 2014, pp. 1–5.
[48] E. Yuan, W. Qi, P. Liu, L. Wei, L. Chen, Ranging method for navigation based on high-speed frequency-hopping signal, IEEE Access 6 (2017) 4308–4320.
[49] Y. Zhou, P. Zammit, V. Zickus, J.M. Taylor, A.R. Harvey, Twin-airy point-spread function for extended-volume particle localization, Phys. Rev. Lett. 124 (19) (2020) 198104.
[50] Y. Wang, W. Zhu, W. Qi, J. Xu, G. Fan, R. Wang, X. Li, Super-resolution imaging of multiple defects in metal thin plates using phased array ultrasonic lamb waves, Mech. Syst. Signal Process. 237 (2025) 113094.
[51] C. Holmes, B.W. Drinkwater, P.D. Wilcox, Post-processing of the full matrix of ultrasonic transmit–receive array data for non-destructive evaluation, NDT & E Int. 38 (8) (2005) 701–711.